Alma Mater Studiorum – Università di Bologna

Dipartimento di Fisica e Astronomia "Augusto Righi"
Laurea Magistrale in Fisica del Sistema Terra

Understanding Inter-model Spread in Arctic Warming: Insights from a Conceptual Model

Presentata da:
Giulia Martini

Relatore:
Dott. Paolo Ruggieri

Correlatore:
Dott. Guillaume Gastineau

Anno Accademico 2024 - 2025
Appello V

Contents

Abstract

The Arctic is warming up to four times faster than the global mean, a phenomenon known as Arctic amplification (AA). AA is a robust feature of CMIP6 models, but projections show large inter-model spread, leaving its mechanisms uncertain. This accelerated warming results from local and remote processes contributing to projection differences. This thesis investigates the processes controlling Arctic warming and the source of the inter-model spread in AA. Diagnostics from climate models are combined with a reduced complexity conceptual model. Three CMIP6 general circulation models (GCM) with different degrees of AA are analyzed. AA is quantified from near surface temperature anomalies and feedback contributions are estimated with a radiative kernel method. The analysis shows that models with stronger AA reproduce observed Arctic warming more realistically, while models with weaker amplification underestimate Arctic and global temperature changes. Model differences are linked to Arctic feedback processes. Surface albedo and lapse rate feedbacks emerge as dominant contributors to Arctic warming and to the inter-model spread. A vertically resolved single column conceptual model of the Arctic climate system is used to further investigate model differences. The model simulates the coupled evolution of the ocean mixed layer, sea ice and atmosphere and is calibrated with parameters from the analyzed GCMs. It reproduces the relative differences in Arctic warming and sea ice loss across the three GCMs. Mechanism denial experiments isolate the role of individual processes. Results show that within the conceptual framework lapse rate and water vapor feedbacks exert the strongest control on Arctic temperature changes. Reduced complexity models can capture key features of climate system evolution, reproducing the inter-model spread encoded in the calibration parameters. A simplified framework helps interpret Arctic warming mechanisms and sources of uncertainty in AA projections.

Chapter 1

Introduction

1.1 Arctic Amplification

Arctic amplification is defined as the phenomenon of the enhancement of near surface air temperature change in the Arctic relative to lower latitudes and the global mean. This is a feature that is readily apparent in observations over recent decades (Previdi et al. 2021). As far back as 1896, the Swedish scientist Svante Arrhenius hypothesized that changes in the concentration of carbon dioxide in Earth's atmosphere could alter surface temperatures. He also suggested that changes would be especially large at high latitudes. Since the mid-20th Century, average global temperatures have warmed 1.19 °C since pre-industrial climate (NASA 2024), but near surface temperature has increased from 2 to 4 times faster in the Arctic than the rest of the globe (Rantanen et al. 2022). According to the National Snow and Ice Data Center, in March 2025 Arctic sea ice reached a record-low winter maximum extent of 14.31 million square kilometers, reflecting the long term declining trend of approximately 40,000 square kilometers per year since 1979 (NOAA 2024). Figure 1.1 shows the linear trends in annual mean surface air temperature over the 50 years preceding 2025. The inset displays the trends averaged by latitude, revealing that warming at higher latitudes is up to about four times faster than in the rest of the globe. Increasing atmospheric greenhouse gases concentration and the related global warming (Notz et al. 2016) are causing the ongoing rapid retreat of Arctic sea ice (Parkinson 2022) with large consequences on ecosystems and human activities (IPCC 2019). The US National Oceanic and Atmospheric Administration has issued in 2025 its annual Arctic Report Card, it documents new evidence that warming of the air, ocean and land is affecting people, ecosystems and communities across the Arctic region (Druckenmiller et al. 2025). The current state of the Arctic climate, the damaged nature of ecosystems and the effects that changes Arctic sea ice cover has on the rest of the globe make it essential to deeply understand the mechanisms driving warming in this region, so as to reduce uncertainty about future projections. A clear vision of what is likely to happen is essential for implementing adaptation policies (Kivimaa et al. 2024).

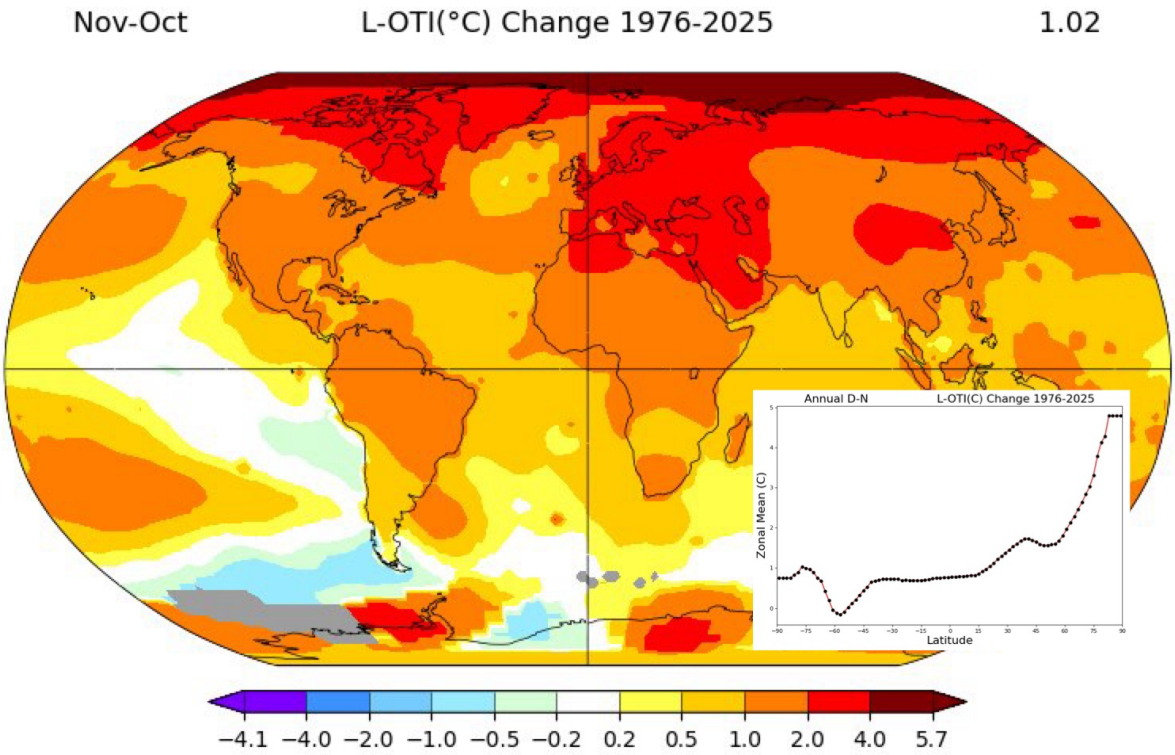

Figure 1.1: Linear trends in annual mean surface air temperature for the period 1976–2025, based on the National Aeronautics and Space Administration Goddard Institute for Space Sciences temperature analysis (NASA Goddard Institute for Space Studies 2024). The inset shows linear trends over the 50-year analysis period averaged by latitude.

The mechanisms that enhance Arctic warming can be categorized into remote forcing and local processes. Remote forcings includes changes in atmospheric or oceanic poleward energy transport from lower latitudes which includes atmospheric moisture transport from lower latitudes (Mewes et al. 2019). Factors linked to climate variability and dynamics also contribute (Sweeney et al. 2024). Henderson et al. (2021) gives a review of the local and remote drivers of Arctic Amplification focusing on the role of high-latitude atmospheric blocking, poleward moisture transport, and tropical and high latitude subseasonal teleconnections, stressing the importance of capturing tropical to Arctic teleconnections to understanding the enhanced Arctic warming. Local processes include processes such as greenhouse gas increase, cloud cover change, albedo changes, lapse rate feedback, and changes in surface heat and moisture fluxes from the Arctic Ocean. Surface warming is closely linked to diminishing sea ice cover (Screen et al. 2010; Screen et al. 2012).

Polar amplification exhibits a pronounced seasonal cycle, with a minimum warming over the Arctic during summer and a maximum warming in autumn and winter (Goosse et al. 2018; Serreze et al. 2026). Figure 1.2, reproduced from Serreze et al. (2026), shows the linear trends in ERA5 2-m air temperature by season. The analysis of observed Arctic amplification over the past 40 years highlights a stronger signal during the cold season (Serreze et al. 2026). Most of the processes that influence the seasonal signature of Arctic amplification are local feedbacks. In summer, the strong positive surface albedo feedback is largely compensated by enhanced ocean heat uptake and by negative cloud feedbacks. In contrast, during autumn and winter, the release of heat stored in the ocean, together with the contributions from the lapse rate feedback and cloud feedbacks, leads to substantial Arctic warming (Laîné et al. 2016; Goosse et al. 2018; Ono et al. 2022). According to the National Snow and Ice Data Center, Arctic sea ice declines more strongly from September to March than during summer, thereby amplifying wintertime warming. While the ice albedo feedback acts primarily in late summer, the subsequent release of oceanic heat to the atmosphere acts in late autumn (Ono et al. 2022). More recently Graff et al. (2025) refined the understanding of the interactions between ocean warming and cloud changes in the Arctic, emphasizing that these coupled processes require further investigation. They identified ocean heat uptake and its subsequent release as the dominant contributor to winter Arctic warming. Other studies (Bintanja et al. 2011; Linke et al. 2023; Pithan et al. 2014) have highlighted the role of strong thermal inversions and the associated reduction in infrared cooling to space as key contributors to amplified Arctic winter warming. While the surface albedo feedback and strong atmospheric stratification at high latitudes remain the leading explanations for polar amplification in most of the past literature (Serreze et al. 2011), recent studies emphasize the role of coupled atmosphere, ocean, sea and ice processes (Chung et al. 2025).

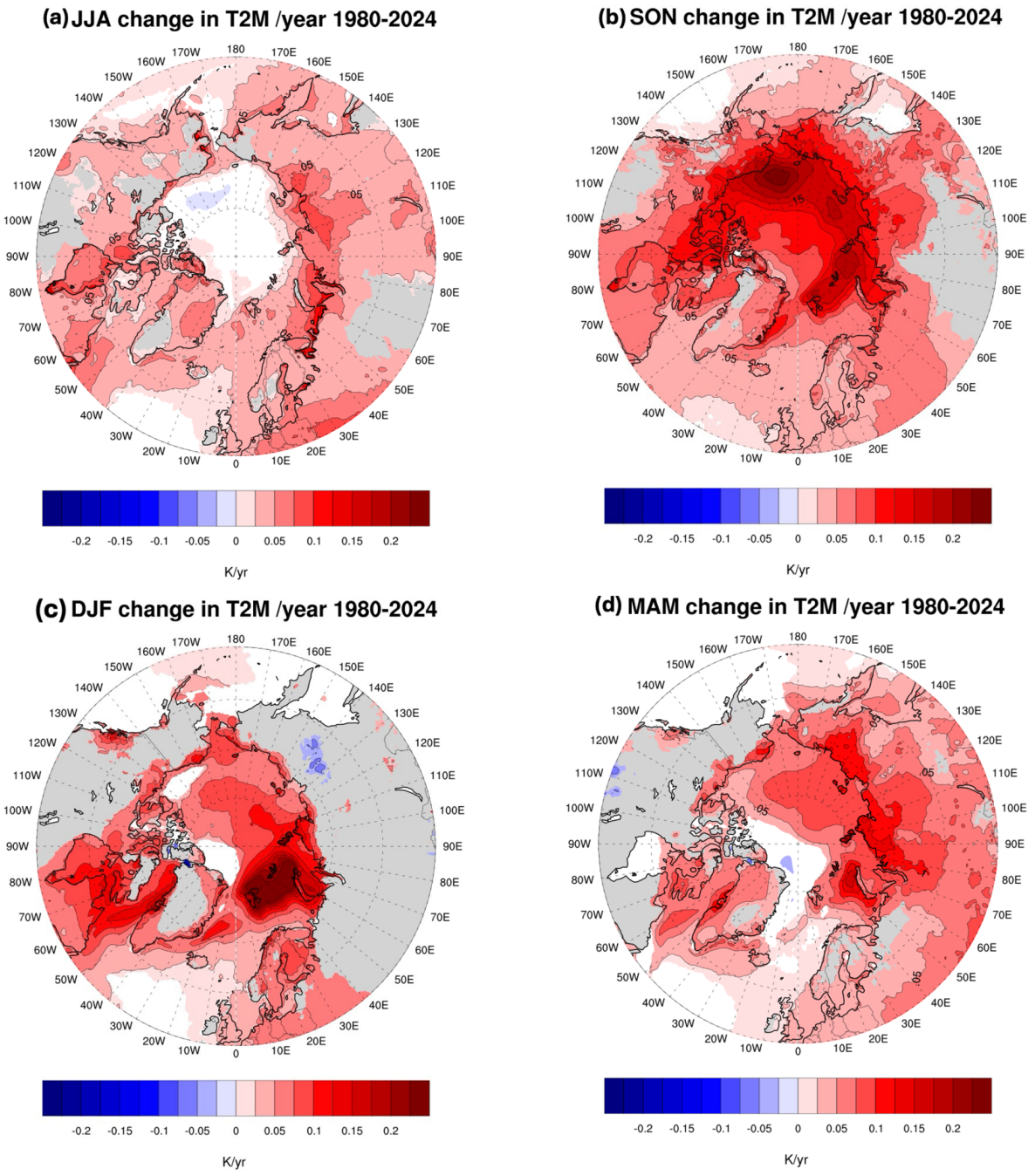

Figure 1.2: Linear trends in ERA5 2-m temperatures by season from 1980 to 2024, in degrees per year for (a) June, July, August (JJA), (b) September, October, November (SON), (c) December, January, February (DJF) and (d) March, April, May (MAM). Only trends significant at $p < 0.05$ are shaded based on an ordinary least squares regression test. The figure is reproduced from Serreze et al. (2026)

Arctic Amplification in Climate Models

Climate model projections consistently show enhanced surface warming in the Arctic relative to the global mean (Holland et al. 2003). In recent generations of climate models, improvements in the representation of Arctic processes have led to a better simulation of observed warming patterns. In particular, CMIP6 models generally reproduce the observed wintertime and near surface amplified warming more accurately than CMIP5 models (Hahn et al. 2021). Despite these advances, significant discrepancies remain in the magnitude and mechanisms of Arctic amplification emerging in the presence of both inter-model and intra-model spread among CMIP6 models AA degree. Within the CMIP6 ensemble, different models show substantial differences in projected Arctic warming, sea ice decline, and coupling with midlatitude climate (Cohen et al. 2020). A graphical example of this discrepancy is shown in figure 1.3, where the annual mean near surface temperature simulated by individual CMIP6 models is displayed for the period from 1900 to 2060. The figure compares Arctic and global temperatures, highlighting an inter-model spread of up to 6 K in future Arctic projections, compared with a spread of about 2.5 K in the global mean temperature. These discrepancies arise from differences in internal climate variability, model formulation, and the representation of physical processes. Internal variability alone can explain a significant fraction of the spread in near surface temperature and sea ice concentration trends (Ye et al. 2021), while differences in model physics, particularly sea ice processes and ocean-atmosphere interactions, further contribute to model divergence (Zhang et al. 2023). A number of studies have investigated the physical drivers of this spread. Surface albedo feedback is consistently identified as the dominant contributor to Arctic amplification and its inter-model spread, followed by lapse rate feedback (Pithan et al. 2014; Hahn et al. 2021). Changes in poleward atmospheric heat transport and water vapor feedbacks also play an important role, although moist transport effects are partially offset by dry transport processes (Hahn et al. 2021; Zhang et al. 2023). Differences in the spatial patterns of sea ice retreat (Boeke et al. 2018) and in the timing of seasonal melt, particularly in early summer (Hu et al. 2022), have been found strongly influence of Arctic surface warming. In some other studies sea ice loss alone cannot fully explain the magnitude of Arctic warming. Those studies highlighting the role of deep Arctic warming suggest that additional processes, including atmospheric structure and energy redistribution, are required to account for model discrepancies (He et al. 2020; Labe et al. 2020). Process based analyses emphasize the importance of coupled mechanisms. Stolla et al. (2023) identify a chain of processes linking increased incoming longwave radiation, enhanced non shortwave heat fluxes both in the surface energy budget, and subsequent sea ice loss. In this framework, clouds have been found with a relatively minor role in explaining inter-model variability in longwave radiation, while Arctic temperature increases and water vapor feedbacks are more influential. Other studies identify clouds as the main source of uncertainty in Arctic climate projections (Bonan et al. 2025; Coulbury et al. 2024). Earlier work on CMIP5 models (Boeke et al. 2016) similarly attributes model spread to changes in the efficiency of the Arctic system in dissipating excess heat, linked to thinner sea ice and a strengthened ice albedo feedback, as well as

to seasonal ocean heat storage and release. Remote influences also contribute to Arctic amplification uncertainty. Poleward energy transport and large scale circulation changes affect the Arctic energy budget (Zhang et al. 2023), and targeted experiments such as the Polar Amplification Model Intercomparison Project (PAMIP) have been designed to isolate the relative roles of local sea ice loss and remote sea surface temperature anomalies (Smith et al. 2019). Despite these efforts substantial model discrepancies remain, including disagreement in the sign of total Arctic radiative feedback in CMIP5 models, which has been linked to differences in initial sea ice conditions and surface temperature responses (Block et al. 2020). A recent study suggests that part of the discrepancy in simulated Arctic amplification may originate from an overestimation of global temperature trends in climate models.Chylek et al. (2024) show that CMIP6 models tend to overestimate global mean warming since the 1990s, which leads to an underestimation of Arctic amplification. When global temperature trends are constrained to observations, simulated AA agrees more closely with observations. In other studies differences in the representation of Arctic warming and feedback processes remain a key source of inter-model spread (Linke et al. 2023). Further work is needed to better understand the role of these processes in driving Arctic warming and amplification, and to reduce uncertainties in future projections (Serreze et al. 2026).

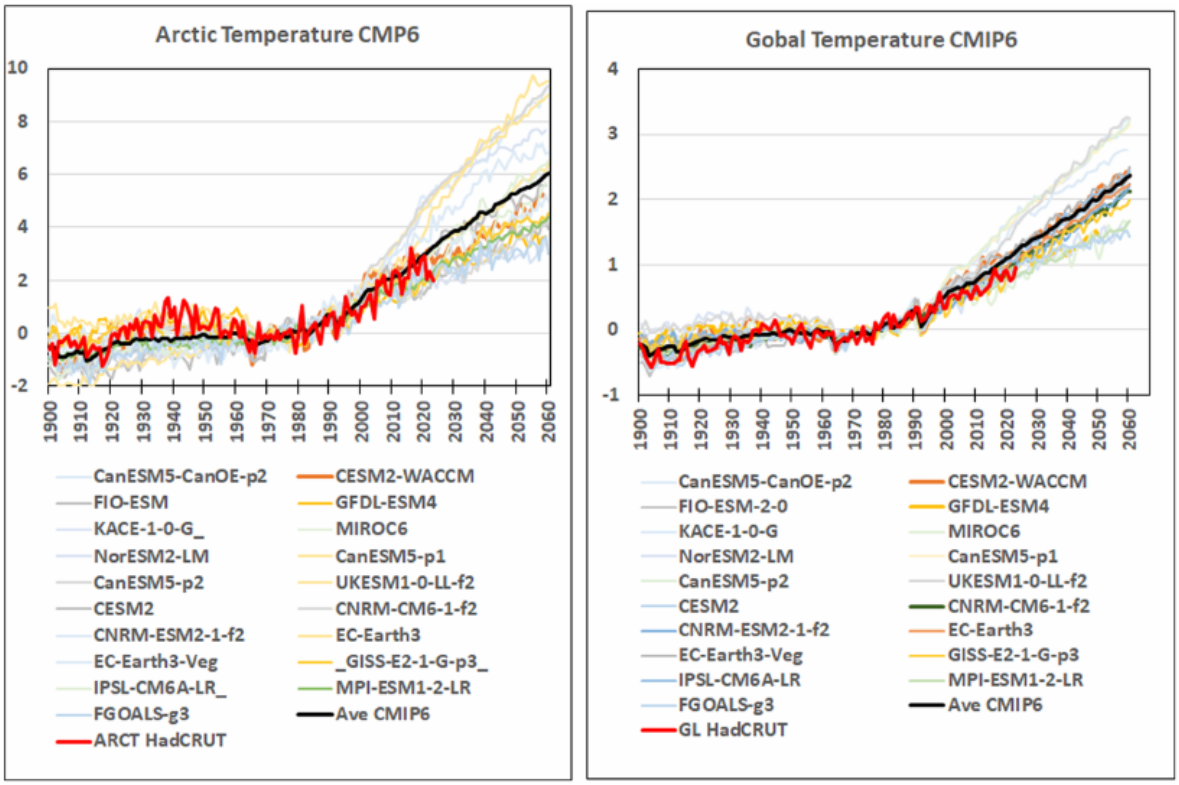

Figure 1.3: (a) Arctic observed temperature (thick red line), temperature simulated by individual CMIP6 models (thin colored lines), and CMIP6 models mean (thick black line). The models' simulations are extended till the year 2060. The range of models' projections of the Arctic temperature anomaly in the year 2060 is from 3°C to 9°C. (b) The observed mean global temperature (thick red line), mean of CMIP6 simulations (black thick line), and mean of individual models (thin color lines) (Chylek et al. 2024).

1.2 Feedback Processes in the Arctic Climate System

The concept of climate feedback is used to interpret the response of the climate system to external forcing. the term feedback is not uniquely defined in climate science and different definitions can lead to different interpretation of the same physical processes (Bates 2007; Feldl et al. 2013; Goosse et al. 2018). Bates (2007) makes a distinction between definition of feedbacks that highlight the impact on the stability of the climate system and those that highlight the impact on the sensitivity to forcing of the climate system. Stability-altering feedbacks describe how the system responds to small perturbations around an equilibrium state, determining whether these perturbations grow or decay over time (Stommel 1961). In this framework feedbacks are closely related to the dynamical properties of the system and are analogous to the concept of feedback in control theory, where negative feedbacks promote

stability and positive feedbacks can lead to instability (Bates 2007; Hansen et al. 1984).

Sensitivity-altering feedbacks refer to processes that modify the amplitude of the equilibrium temperature response to a given external forcing. In its simplest representation, the response of the climate system to a perturbation can be described by a linear energy balance model:

$$c_0 \frac{dT'}{dt} = F' - \lambda T' \tag{1.1}$$

where T' is the temperature perturbation, F' represents the external radiative forcing, and c_0 is an effective heat capacity of the climate system. The parameter λ represents the net radiative response of the climate system to a temperature perturbation and therefore implicitly includes the damping or amplifying effects of climate feedback processes (Bates 2007). At equilibrium the temperature response becomes

$$\Delta T = \frac{\Delta F}{\lambda} \tag{1.2}$$

These feedbacks affect the magnitude of the equilibrium temperature response. This is the definition used in the IPCC assessment (Matthews et al. 2021) and in the traditional climate feedback framework used in radiative kernel analysis (Lu et al. 2009; Crook et al. 2011; Feldl et al. 2013; Taylor et al. 2013; Pithan et al. 2014; Goosse et al. 2018; Hahn et al. 2021; Linke et al. 2023). Difficulties in the definition of feedback have been identified as one of the impediments to progress, pointing out that different assumptions about the nature of the climate system can lead to feedback measures that differ not only in magnitude but also in sign (Bates 2007). Models may agree on the results while attributing them to different underlying causes. Heinze et al. (2019) illustrate this with the example of different feedback mechanisms influencing the same temperature response. In particular, within cloud feedbacks, they note that similar radiative changes can result from variations in cloud amount, reflectivity, height, or water phase. The Arctic climate is shaped by multiple interacting processes operating across different spatial and temporal scales, which contribute to Arctic amplification. The drivers of this enhanced warming remain an active area of research. Here we briefly review the main feedback mechanisms involved and their role in the Arctic climate system. A schematic overview of these processes is shown in figure 1.4, reproduced from Goosse et al. 2018.

Many Arctic feedback processes are linked to the presence of sea ice (Chung et al. 2025). Sea ice insulates the relatively warm Arctic Ocean from the much colder atmosphere for most of the year. When this insulating cover weakens or disappears, heat exchange between the ocean and the atmosphere increases, leading to warming of the overlying air. In response to an initial positive radiative forcing, the summer sea ice melt season lengthens and intensifies. As the ice melts, darker open water areas are exposed and readily absorb solar radiation, increasing the heat content of the ocean mixed layer (Perovich et al. 2007). This additional heat promotes further ice melt because the absence of ice enhances ocean–atmosphere energy exchanges (Jenkins et al. 2021). During the cold season, increased open water and higher ocean

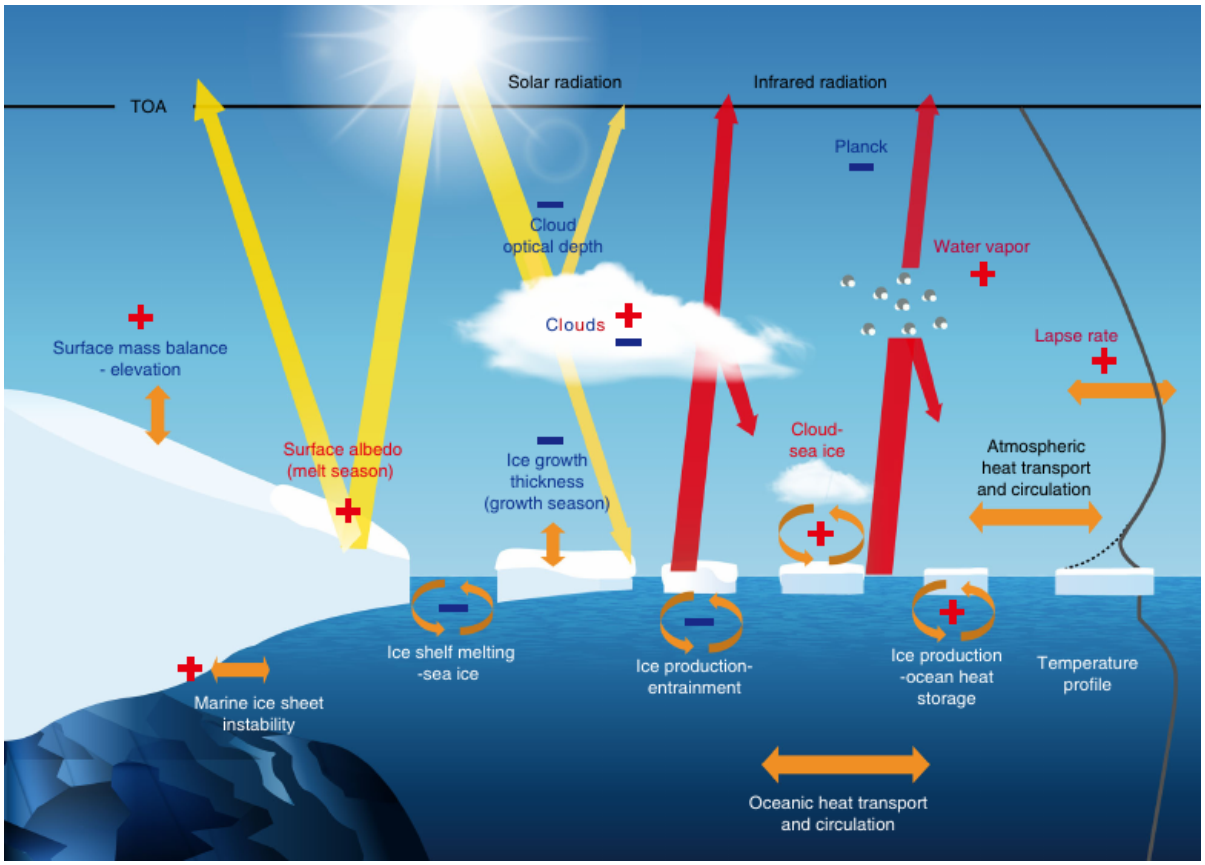

Figure 1.4: A schematic of some important radiative and non-radiative feedbacks acting in polar regions reproduced Goosse et al. (2018). The schematic involve the atmosphere, the ocean, sea ice and ice sheets. In yellow Shortwave and in red longwave radiation exchanges. A red plus sign means that the feedback is positive, a negative blue sign corresponds to a negative feedback. Both signs are present for cloud feedbacks as both positive and negative feedbacks are occurring simultaneously and the net effect is not known. The gray line on the right represents a simplified temperature profile in polar regions for the atmosphere and the ocean, the dashed line corresponding to a strong surface inversion.

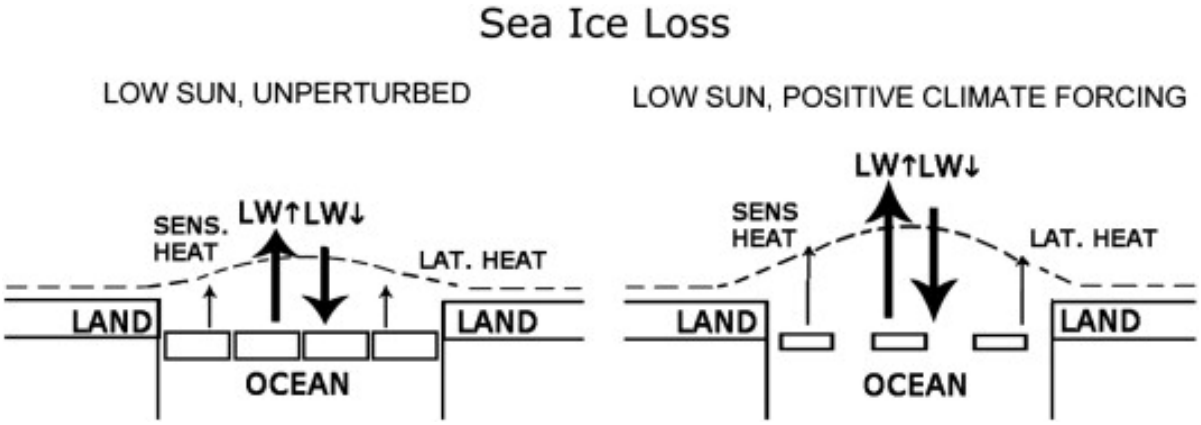

Figure 1.5: Schematics of the surface energy budget of the Arctic Ocean, contrasting the situation during the low-sun period for (left) an unperturbed Arctic and (right) in response to a positive (warming) climate forcing that results in decreased ice concentration and thickness. The dotted line is an arbitrary isotherm in the lower troposphere; warming over the Arctic Ocean bows the isotherm upward. SW = shortwave radiation flux, LW = longwave radiation flux, Sens. Heat = sensible heat flux, Lat. Heat = latent heat flux. Figure reproduced from Serreze et al. (2011).

heat content enhance upward heat fluxes through longwave radiation and turbulent latent and sensible heat exchanges with the atmosphere. In winter latent heat release associated with sea ice growth also contributes to upward heat fluxes; thinner ice formed under these conditions melts more easily the following summer. A schematic representation of these energy flux changes associated with sea ice loss is shown in figure 1.5.

Melting ice and snow lower surface albedo, increasing shortwave absorption and amplifying warming (Goosse et al. 2018). The surface albedo in the Arctic ranges from 0.8 for ice that is at least 1 meter thick, to around 0.1 for open ocean (Hall 2004). The warmer surface emits more longwave radiation and enhances turbulent heat fluxes, increasing air temperature and the longwave radiation flux back to the surface (Serreze et al. 2011). The Arctic amplification signal linked to sea ice loss can be viewed as a delayed seasonal expression of albedo feedback (Serreze 2008; Winton 2006).

For the atmospheric horizontal energy fluxes the Arctic region is characterized by both moisture and heat transport; in the annual mean, this convergence is primarily balanced by longwave radiation loss to space. Variations in heat and moisture flux convergence affect Arctic temperature by altering atmospheric water vapor and cloud cover, which influence surface energy balance through greenhouse effects and modulation of incoming solar radiation. Changes in heat flux convergence also impact sea ice extent and surface albedo (Serreze et al. 2011). Regarding impacts of ocean circulation, Chylek et al. (2009) showed that Arctic air temperature changes are linked to the phase of the Atlantic Multi-decadal Oscillation (AMO). The AMO describes a multi-decadal oscillation in North Atlantic sea surface temperatures,

with the largest changes at high latitudes. Under global warming scenarios the warmer atmosphere can hold more moisture, which leads to an increase in latent energy transport. The polar amplification decreases the equator to pole temperature gradient, which decreases the dry static energy transport. This compensation is seen in both energy balance models (Hwang et al. 2011) and general circulation models (Hwang et al. 2010).

At high latitudes, stable stratification leads to stronger warming in the lower than in the upper troposphere, producing a positive lapse rate feedback. A vertically nonuniform warming alters the infrared irradiance to space relative to that of a vertically uniform tropospheric warming (Boeke et al. 2021). The lapse rate feedback is negative at low latitudes, as a result of moist convective processes, and positive at high latitudes, due to stable stratification conditions that effectively trap warming near the surface (Goosse et al. 2018; Pithan et al. 2014). It is shown that this feedback pattern leads to polar amplification of the temperature response induced by a radiative forcing (Graversen et al. 2014; Linke et al. 2023; Pithan et al. 2014; Boeke et al. 2021; Feldl et al. 2017). Other studies affirm that lapse rate feedback has a neutral effect on Arctic amplification by cooling the Arctic and the tropics by approximately equivalent amounts (Beer et al. 2022).

The longwave radiation emitted by the Earth's surface rises with temperature following the Stefan Boltzmann law. Thus a given increase in emitted radiation requires a larger temperature increase at colder background temperatures. Because colder regions emit less longwave radiation per degree of warming, the Planck response is weaker in the Arctic than in the tropics, which contributes to Arctic amplification (Henry et al. 2020; Pithan et al. 2014).

In a warming climate, the amount of water vapor in the atmosphere increases, which amplifies the greenhouse effect and leads to further warming (Curry et al. 1995). An increase in atmospheric water vapor and total cloud cover led to greenhouse effects larger in the Arctic than at lower latitudes, linked in part to the stably stratified conditions that often prevail in the Arctic which inhibit mixing (Goosse et al. 2018). Screen et al. (2026) show that water vapor feedback contributes to Arctic warming but opposes amplification due to larger tropical than Arctic moistening under sea surface temperature induced warming with fixed Arctic sea ice. An approach of inactivating individual feedback processes during forced warming and evaluating the resulting change in the surface temperature field conducted by Beer et al. (2022) reveals that when warming is attributed to each feedback process by comparing how the climate would change if the process were not active, the water vapor feedback is the primary reason that the Arctic region warms more than the tropics.

Clouds have both warming and cooling effects on the Arctic climate, as it is shown in figure 1.4. They reduce the shortwave flux to the surface through their high albedo, and cloud cover (especially low-level Arctic stratus) augments the downward longwave flux to the surface; key factors influencing the longwave emission are cloud base temperature and whether the cloud cover is liquid phase, mixed phase or ice phase (Liu et al. 2008; Heinze et al. 2019). Kay et al. (2016) conduct a study based on direct observations. They shows that clouds warm the surface except for a brief period in summer, the surface net all-wave radiation flux is larger in the presence of cloud cover as compared to clear sky conditions. The net surface warming in

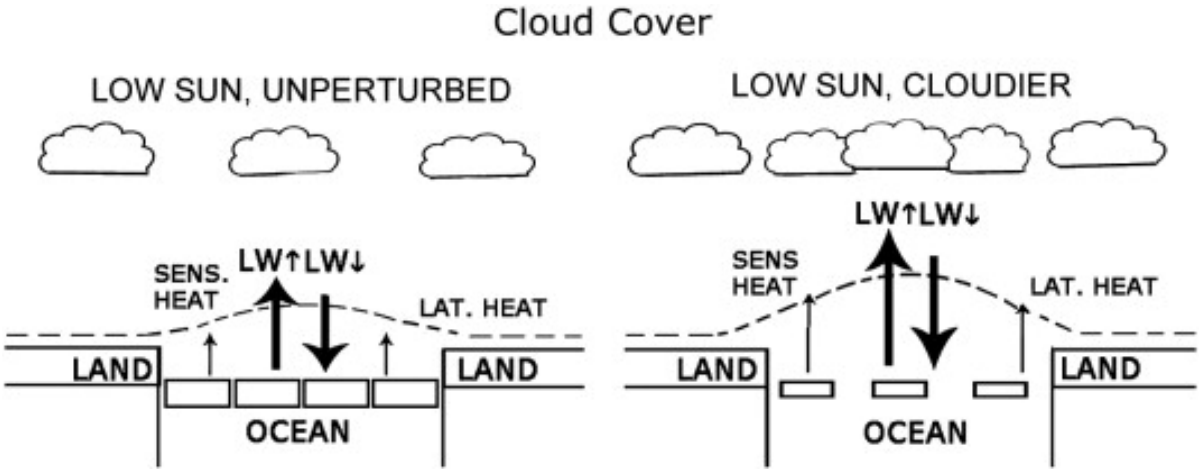

Figure 1.6: Schematics of the surface energy budget of the Arctic Ocean, contrasting the situation during the low sun period for (left) an unperturbed Arctic and (right) in response to a forcing that results in more extensive and/or thicker cloud cover. The dotted line is an arbitrary isotherm in the lower troposphere; warming over the Arctic Ocean bows the isotherm upward. Changes in water vapor content linked to changes in open water fraction may contribute to temperature change. SW = shortwave radiation flux, LW = longwave radiation flux, Sens. Heat = sensible heat flux, Lat. Heat = latent heat flux. The figure is reproduced from Serreze et al. (2011).

the Arctic for most of the year is due to the absence of solar radiation during polar night and the high albedo of the sea ice surface (Serreze et al. 2011). The warming effect of clouds at the surface of the Arctic contrasts with lower latitudes, where clouds have a net cooling effect (Vavrus et al. 2011). Sea ice loss increases atmospheric moisture, which can enhance cloud formation (Serreze et al. 2011). A schematic representation of the radiative impact of cloud cover under low-sun conditions is shown in figure 1.6.

The ocean acts as an energy reservoir that transports and releases heat within the Arctic climate system (Timmermans et al. 2020). The ocean exerts a stabilizing influence by storing heat in the upper ocean during summer, temporarily delaying atmospheric warming. Oceanic heat transport is shown in fig. 1.4 but without signs as the processes involved are not restricted to polar regions and it is not clear if they could be formally expressed using a closed feedback loop (Goosse et al. 2018). A contribution to Arctic warming comes from poleward ocean heat transport, which carries warmer waters from lower latitudes into the Arctic. This occurs through Atlantic inflow via the Barents Sea Opening and Fram Strait (Smedsrud et al. 2010), and Pacific inflow through the Bering Strait (Xu et al. 2024). These processes contribute to Arctic Ocean warming and sea ice decline commonly referred to as Atlantification and Pacification. The relative magnitude and individual impacts of these two heat transport pathways remain uncertain (Cheng et al. 2025). Atlantification is associated with pronounced ocean

warming, weakened upper ocean stratification, and reduced winter sea ice, particularly in the Barents Sea, the eastern Eurasian Basin, and the adjacent Kara and Greenland seas (Boitsov et al. 2012; Matishov et al. 2014; Polyakov et al. 2017; Schlichtholz et al. 2019). As Atlantic waters enter the Arctic, heat is partly stored in the upper ocean and partly released to the atmosphere through surface fluxes. This release is strongest in winter, when the temperature contrast between the relatively warm ocean and the cold overlying air enhances turbulent heat exchange (Ivanov et al. 2015; Tetzlaff et al. 2013). Ice covered regions inhibit turbulent heat fluxes, while open water areas allow strong coupling between the ocean and atmosphere (Vihma 2014). When openings in the ice cover develop along the Atlantic Water pathway, weak stratification at the base of the mixed layer can trigger thermohaline convection. This process entrains warmer and saltier water from deeper layers, increasing upward heat flux. As a result, ice formation is delayed, ice thickness remains reduced, or ice formation may be completely suppressed (Ivanov et al. 2015). In addition to its role in heat transport, the ocean also acts as a seasonal heat reservoir. During summer solar radiation is absorbed and stored in the upper ocean, and this heat is subsequently released in autumn and winter. This seasonal storage and release of heat contributes to the asymmetric Arctic warming, with stronger warming occurring during the colder months (Smedsrud et al. 2010).

Methods to Quantify Feedbacks

The quantitative evaluation of climate feedbacks is commonly based on the radiative feedback framework, which relates changes in the Earth energy balance to variations in near surface temperature. Within this framework feedback parameters λ_i are defined as the change in radiative flux associated with a perturbation in a given climate variable, normalized by the change in surface temperature and expressed in W m^{-2} K^{-1}. The net feedback parameter is obtained as the sum of all individual contributions and can be estimated either from the global energy balance or through regression of top of the atmosphere (TOA) radiative flux anomalies against global mean surface temperature changes (Gregory et al. 2004). Diagnosing individual feedbacks requires isolating the contribution of each variable to the radiative budget, which is not trivial because of the strong coupling among climate processes (Wetherald et al. 1988; Taylor et al. 2007; Soden et al. 2008; Shell et al. 2008). TOA radiative flux anomalies are approximated as a linear superposition of contributions from changes in state variables associated with specific feedback mechanisms. Radiative kernels quantify the sensitivity of radiative fluxes to perturbations in each variable, allowing feedback parameters to be estimated by combining these sensitivities with simulated changes in the corresponding variables (Pendergrass et al. 2017; Soden et al. 2006; Soden et al. 2008; Shell et al. 2008). Alternative approaches include partial radiative perturbation methods and related approximations, which follow a similar conceptual framework but are computationally more demanding (Taylor et al. 2007).

TOA fluxes provide a convenient reference for global feedback analysis but their interpreta-

tion can be more complex in the Arctic. Strong stability in the lower troposphere limits vertical mixing, so feedbacks diagnosed at the surface may differ substantially from those inferred at TOA (Pithan et al. 2014; Taylor et al. 2013; Laîné et al. 2016). For example, Goosse et al. (2018) highlight that cloud-induced changes in atmospheric emissivity may produce opposite feedback signs at the surface and at TOA, emphasizing the importance of considering multiple diagnostic levels.

Another metric used to quantify feedbacks is the feedback factor γ_i, defined as the ratio between the additional change due to a specific feedback and the response of the full system including all feedbacks of a selected variable. This dimensionless formulation allows comparisons across different feedback processes and models, its value depends on the chosen reference state (Goosse et al. 2018).

A three-dimensional diagnostic approach, known as the Climate Feedback Response Analysis Method (CFRAM), attributes temperature changes to different processes at various atmospheric levels, providing insights into the vertical structure of feedbacks and their interactions. This method is particularly useful for investigating processes such as lapse rate feedback but requires highly detailed model output (Taylor et al. 2013).

Several alternative decompositions of climate feedbacks have also been proposed, highlighting that different methodologies may yield different quantitative estimates (Laîné et al. 2016; Feldl et al. 2013; Beer et al. 2022). A key limitation of the standard radiative feedback framework is the assumption that feedbacks scale linearly with surface temperature. This approximation is useful but it can be violated because the climate response may be non-linear and depend on the magnitude of the perturbation or on the mean state of the system (Mitchell et al. 1989; Feldl et al. 2013; Andrews et al. 2015; Colman et al. 2011; Meraner et al. 2013; Gregory et al. 2015). In polar regions these non-linearities are particularly relevant due to phase changes of water and the strong coupling of ocean, ice and atmosphere (Zelinka et al. 2012; Goosse et al. 2018). The radiative framework struggles to account for non-radiative feedbacks, such as those related to ocean–ice interactions, whose quantification remains less standardized. Examples include the ice thickness growth feedback, defined through the sensitivity of ice thickness to external forcing (Bitz et al. 2004), as well as feedbacks involving ice production, entrainment processes, and ocean heat storage, which can be estimated from ratios of heat fluxes or volume changes (Martinson 1990; Goosse et al. 2014; Lecomte et al. 2017). The diversity of definitions complicates comparisons across studies and highlights the need for more unified diagnostic approaches.

Alternative experimental strategies have been developed to isolate the role of specific feedback mechanisms. Mechanism denial experiments quantify the contribution of a given feedback by artificially suppressing it in a climate model and comparing the resulting response with a control simulation. This approach accounts for interactions among processes but it is computationally expensive (Hall 2004; Graversen et al. 2009; Beer et al. 2022; Hankel et al. 2023). Simplified models, offer a computationally efficient framework for exploring feedback interactions and the role of atmospheric heat transport (Hwang et al. 2011; Rose et al. 2014; Bonan et al. 2018). Studies using these approaches emphasize that feedbacks and heat trans-

port are not independent processes, and that their interactions are particularly important for understanding Arctic amplification (Henry et al. 2020; Beer et al. 2022).

Different methodologies therefore provide complementary perspectives on climate feedbacks. When combined with climate models of varying complexity, these diagnostic approaches offer multiple pathways to quantify feedback processes and to analyze the climate system from different methodological perspectives.

1.3 Models of different complexity

Climate models simulate Earth system climate by representing many physical processes and solving numerically the equations of the fluid mechanics. Building and running a climate model requires identifying and quantifying Earth system processes, representing them mathematically, defining initial conditions, and solving the governing equations defining appropriate boundary conditions. Models span a hierarchy of complexity, reflecting compromises between physical realism, interpretability and computational costs (Claussen et al. 2002). At the highest level of complexity, General Circulation Models (GCMs) provide a comprehensive representation of the climate system. They simulate the coupled dynamics of the atmosphere, ocean, cryosphere, and land surface by solving the fundamental equations of fluid dynamics and thermodynamics (Khan et al. 2025). The theoretical foundations of GCMs can be traced back to the primitive equations formulated in the early 20th century, and their development has progressed alongside advances in process understanding and computational capacity (Weart 2010). GCMs today are the most advanced tools available for simulating global climate, the response of the climate system to external forcings, including greenhouse gas emissions, land use changes, and biogeochemical processes (Ackerman et al. 2006; Donner et al. 2011; McKenney et al. 2011). GCM simulations are coordinated within the Coupled Model Intercomparison Project (CMIP) (World Climate Research Programme (WCRP) 2026), with successive phases from CMIP1 to CMIP6 incorporating increasing levels of complexity and improved process representation (Flato 2011; Sperber et al. 2013). The latest generation is CMIP6 and it includes higher spatial and temporal resolution and new forcing scenarios such as the Shared Socioeconomic Pathways (SSPs), which integrate socioeconomic development, technological changes, and land use evolution (Fernandez-Granja et al. 2021; Moss et al. 2010). Despite their realism, GCMs are affected by significant uncertainties arising from differences in model structure, parameterizations, and internal variability (Iqbal et al. 2020). These uncertainties contribute to substantial inter-model spread, particularly at regional scales, and often require model selection or evaluation against observations for specific applications (Chylek et al. 2009; Hahn et al. 2021). Moreover, the strong coupling between processes in GCMs makes it difficult to isolate the role of individual mechanisms and to attribute differences across models to specific physical causes. Earth System Models of Intermediate Complexity (EMICs) provide a compromise between realism and computational efficiency. They describe the dynamics of the atmosphere and ocean in less detail than GCMs, either through reduced spatial resolution or simplified dy-

namics, while still retaining a physically based representation of large scale processes (Weber 2010). EMICs include additional components of the climate system compared to simpler models, such as ice sheets, vegetation, and biogeochemical cycles, enabling the study of long term feedbacks and slow climate variability. Their relatively low computational cost allows for large ensemble simulations and long integrations, making them particularly suitable for investigating climate variability from rapid events to glacial interglacial cycles (Weber 2010). Despite being simpler than GCMs, EMICs remain relatively complex and can still be difficult to disentangle the role of individual processes. The least complex type of model are the conceptual models, which reduce the climate system to a limited number of variables and processes (Claussen et al. 2002). These models are often formulated as energy balance models (EBMs) or box models, where the system is represented as homogeneous reservoirs connected by fluxes. EBMs solve the radiative heat balance of the atmosphere and can be formulated in different dimensional configurations (Budyko 1961; Sellers 1969; North et al. 1981), while ocean box models represent density driven circulation between reservoirs and have been used to study multiple equilibrium states of the ocean circulation (Stommel 1961). Conceptual models are computationally efficient and often allow analytical solutions, making them particularly useful for understanding fundamental processes and equilibrium states, allowing controlled experiments that are not feasible in GCMs. Their simplicity enables systematic sensitivity analyses and the isolation of individual mechanisms (Beer et al. 2022). In Arctic climate studies, conceptual models have been used to investigate sea ice dynamics (Haine 2021) and feedbacks (Feldl et al. 2021; Jenkins et al. 2021; Hankel et al. 2023). Their results depend strongly on model formulation (Eisenman et al. 2009; Wagner et al. 2015). Conceptual models have also used to investigate Arctic amplification and its controlling mechanisms (Payne et al. 2015; Goodwin et al. 2023). The diversity of modeling approaches used in studies of Arctic climate gives different insights on the problem of the understanding of such a complex system: comprehensive models provide realistic simulations but limited interpretability, while simplified models allow process level understanding at the expense of physical detail. These complementary abilities motivate the use of multiple modelling approaches to investigate the mechanisms controlling Arctic warming and its variability across models.

1.4 Objective of the Study

Until now Arctic amplification has been extensively studied using comprehensive climate models and observational analysis focusing on the main characteristics of Arctic warming. These analysis focused both on remote and local processes and on the role of individual feedback processes (Pithan et al. 2014; Hahn et al. 2021; Linke et al. 2023). The studies on individual feedback processes have highlighted the importance of surface albedo, lapse rate, clouds and both oceanic and atmospheric heat transport, and have shown the presence of a large inter-model and intra-model spread in the magnitude of Arctic warming. The strong coupling between processes in GCMs however makes it difficult to isolate the contribution of

individual mechanisms and to identify which modeling choices are responsible for the differences across models. In this context simplified frameworks have been used to investigate specific processes in isolation, providing insight into feedback mechanisms and their interactions (Payne et al. 2015; Beer et al. 2022; Hankel et al. 2023). These approaches allow for a controlled experiments and analytical interpretation, but are often applied independently from GCM or observational analysis, using thir ability to understand fundamental processes but not to interpret inter-model differences. The present thesis aims to investigate Arctic warming and its inter-model spread by combining GCM diagnostics with a reduced complexity conceptual model. For this purpose three CMIP6 models characterized by different degrees of Arctic amplification are analyzed in order to quantify Arctic warming and to identify the contribution of individual feedbacks and heat transport processes using a pre-computed radiative kernel method (Pendergrass et al. 2017). In parallel a vertically resolved single column model of the Arctic climate system at 80°N is employed to reproduce and interpret the behavior of the GCMs within a simplified setting. The model is imported from Hankel et al. (2023) but is calibrated using GCM derived parameters, allowing the construction of GCM adapted configurations. This approach enables the comparison of different models within a unified framework and the investigation of how variations in key parameters affect Arctic warming. The conceptual model is then used to perform a set of mechanism denial experiments, in which individual feedback processes are suppressed. This allows the role of specific mechanisms to be evaluated in terms of their impact on surface temperature and sea ice, providing a process based interpretation of the differences identified in the selected GCMs. This approach makes a link between complex climate models and simplified representations, allowing Arctic warming to be analyzed under different conditions within a consistent framework and to offer insight into the physical processes controlling its spread across models. Chapter 2 describes the datasets, the metrics to assess Arctic amplification, the radiative kernel methodology and the conceptual model, including its calibration using GCM outputs. Chapter 3 presents the results from the GCM analysis and the conceptual model simulations, focusing on Arctic amplification, Arctic warming and feedback contributions. Chapter 4 discusses the results in the context of previous studies and evaluates the ability of the conceptual model to interpret inter-model differences within a simplified framework. It summarizes then the main conclusions and outlines directions for future work. Chapter 5 provides supplementary material, including details on data preprocessing, radiative kernel implementation, interpolation procedures, and additional information on the conceptual model numerical implementation.

Chapter 2

Data and Methods

2.1 Datasets

2.1.1 Reanalysis Data

We use data from ERA5, the latest atmospheric reanalysis produced by the European Centre for Medium-Range Weather Forecasts (ECMWF). Reanalysis combines model data with observations from across the world into a globally complete and consistent dataset. This principle, called data assimilation, is based on the method used by numerical weather prediction centres, where every so many hours (12 hours at ECMWF) a previous forecast is combined with newly available observations in an optimal way to produce a new best estimate of the state of the atmosphere, called analysis, from which an updated, improved forecast is issued (Hersbach et al. 2020). Reanalysis works in the same way, but at reduced resolution to allow for the provision of a dataset spanning back several decades. Moreover, differently from analysis, reanalysis use the same model (not time-varying) over the entire time period, providing a uniform performance. Ensemble means of monthly 2-m temperature and sea ice cover are used for the entire region north to latitude 66°N; they have a horizontal resolution of 0.5° × 0.5°. Two windows of time have been selected, a reference period from 1951 to 1980 and a modern period from 1985 to 2014. By choosing that time period, we cover the modern era of Arctic warming that has been identified from the second half of the 20th century and that continues into the 21st century (Davy et al. 2018).

2.1.2 CMIP6 Models Data

In their article, Linke et al. (2023) categorized all CMIP6 GCMs according to their degree of Arctic amplification. They defined two groups, CMIP6/s and CMIP6/w, representing models with strong and weak Arctic amplification respectively, based on a difference-based metric. In this study, we aim to analyze the inter-model spread in the representation of Arctic amplification. To this end, we selected three different GCMs: GFDL-ESM4 from the CMIP6/w group,

and IPSL-CM6A-LR and CMCC-CM2-SR5 from the CMIP6/s group. Two models were chosen from the strong Arctic Amplification category in order to investigate both a medium–high and a high degree of Arctic Amplification, respectively CMCC-CM2-SR5 and IPSL-CM6-LR. As CMCC-CM2-HR4 data were not available, in this study CMCC-CM2-SR5 configuration is used instead. For all models, all available ensemble members are included in the analysis.

IPSL-CM6A-LR model is the low-resolution configuration of coupled model developed by the Institut Pierre-Simon Laplace (IPSL) (Boucher et al. 2020) for participation in CMIP6. It includes representations of key components of the climate system: atmosphere, ocean, land surface, and sea ice. The atmospheric component, LMDZ (Laboratoire de Météorologie Dynamique Zoom), runs on a regular horizontal grid of approximately $2.5^\circ \times 1.25^\circ$ and has 79 vertical levels, ranging from near the surface (10 m) to the stratosphere (0.1 hPa). Oceanic processes are represented by NEMO v3.6 (Nucleus for European Modelling of the Ocean), which includes both ocean dynamics and thermodynamics. The land surface is modeled using ORCHIDEE (Organising Carbon and Hydrology In Dynamic Ecosystems), dynamic vegetation and hydrology model. Coupling between these components is handled by OASIS-MCT. Sea ice is simulated using LIM3, the third generation of the Louvain-la-Neuve Ice Model (Rousset et al. 2015), embedded within the ocean model. LIM3 (version 3.6) is a dynamic–thermodynamic sea ice model that employs a multi-category thickness distribution scheme (Vancoppenolle et al. 2009).

GFDL-ESM4 is the fourth generation Earth system model developed at the Geophysical Fluid Dynamics Laboratory (GFDL) and it also contributes to CMIP6. It represents comprehensive interactions among physical climate, atmospheric chemistry, and biogeochemical cycles. The model includes coupled components for the atmosphere, ocean, land surface, and sea ice. The atmospheric component is based on AM4.1 (Zhao et al. 2018a; Zhao et al. 2018b). The horizontal resolution is $1^\circ \times 1^\circ$, with 49 vertical levels. Ocean dynamics are simulated using MOM6 (Modular Ocean Model version 6) (Adcroft et al. 2019), with 75 layers. The ocean grid has a horizontal resolution of 0.5°. The sea ice component is represented by SIS2 (Sea Ice Simulator version 2), a dynamic thermodynamic model that simulates sea ice motion, thickness distribution, and interactions with the ocean and atmosphere (Adcroft et al. 2019). It is fully coupled to the ocean model and shares the same horizontal grid. The land surface is modeled using LM4.1, which includes representations of vegetation dynamics, soil carbon processes, hydrology, and land use (Dunne et al. 2020). Ocean biogeochemistry is represented by COBALT v2 (Stock et al. 2020). Coupling among the atmosphere, land, ocean, and sea ice components is performed through a flux exchange system that ensures conservation of energy and tracers. Exchanges occur at hourly time steps (Dunne et al. 2020).

CMCC-CM2-SR5 is the standard resolution configuration of the CMCC-CM2 coupled climate model developed by the Mediterranean Centre on Climate Change (CMCC). It partecipates in CMIP6. The model includes fully coupled atmosphere, ocean, land surface, and sea ice components, interacting through the CPL7 coupler (Craig et al. 2012). The atmospheric component is based on CAM5 (Community Atmosphere Model) (Neale et al. 2012). Aerosols are treated interactively using the Modal Aerosol Model (MAM3) (CMCC 2016). The model

operates on a horizontal resolution of about 1°, with a regular grid of $0.9° \times 1.25°$ with 30 vertical levels extending up to about 2 hPa. The ocean component is represented by NEMO version 3.6 (Madec et al. 2016), which has a tripolar ORCA grid with 1° resolution (Madec et al. 1996). The vertical structure includes 50 levels. Sea ice is simulated using CICE version 4 , a dynamic thermodynamic model that includes multiple ice thickness categories and accounts for advection, deformation, thermodynamics, and melt pond evolution (Hunke et al. 2008). The sea ice model shares the same horizontal grid as the ocean component and is fully coupled to both the atmosphere and ocean. The land surface is modeled using CLM4.5 (Community Land Model) (Subin et al. 2012), with hydrology, soil thermodynamics, carbon and nitrogen cycles. In the CMCC-CM2-SR5 configuration, all components operate at 1° horizontal resolution. Coupling among components occurs every 30 minutes and hourly for the ocean (Cherchi et al. 2019).

Experiments and Time Periods Considered

From now on we refer to the GCMs with the shorter names: GFDL, IPSL and CMCC.

We chose two different experiments: historical and 1pctco2 to compute AA degrees. Historical experiment is standardized simulations that run models from the pre-industrial era to the present, testing their ability to reproduce observed climate trends (Eby et al. 2013). This experiment has been chosen to try to reproduce Linke et al. (2023) results and to compare results to observations. 1pctCO2 experiment consists of increase atmospheric CO_2 concentration gradually at a rate of 1 percent per year. The concentration of atmospheric carbon dioxide is increased from the global annual mean 1850 value until quadrupling (Community Earth System Model developers and affiliates 2019). This experiment was chosen to investigate the effect of increasing CO_2 concentration alone, compared to the historical simulation. We chose the same reference (1951-1980) and a modern (1985-2014) period as for ERA5 data in the historical simulations. A corresponding period has been chosen for 1pctCO2 experiment, taking a window of 30 years ($\pm$15 years) around the year of the simulation where the CO_2 concentration corresponds to the mean CO_2 concentration in the reference and modern period in the historical experiment. For GFDL and IPSL, these windows are identified from model output using the variable mass of CO_2, selecting the model year closest to the target CO_2 concentration as the center of the window. For CMCC, which does not provide the mass of CO_2, the timing is estimated assuming a 1%/year CO_2 increase from preindustrial conditions $t = \frac{\ln(C/C_0)}{\ln(1.01)}$, where C_0 is the preindustrial CO_2 concentration.

Horizontal Heat Transport

Horizontal heat transport is diagnosed using energy conservation in the atmospheric column and inferring the divergence of meridional heat transport from the difference between top of the atmosphere and surface energy fluxes:

$$\nabla F = R_{\mathrm{TOA}} - R_{\mathrm{Surf}} - r \tag{2.1}$$

where F is the horizontal energy transport, R_{TOA} is the net radiative flux at the top of the atmosphere, R_{Surf} is the net energy flux at the surface, and r is a non-conservation term accounting for model energy imbalances and numerical residuals. This residual term is estimated from the preindustrial control simulation and removed from the budget. The meridional heat transport is then obtained by integrating the zonal mean divergence from the South Pole to latitude φ:

$$\langle F(\varphi)\rangle = \int_{\varphi_{SP}}^{\varphi} \left(\langle R_{\mathrm{TOA}}\rangle - \langle R_{\mathrm{Surf}}\rangle - \langle r\rangle\right) d\phi \tag{2.2}$$

where angle brackets denote the zonal mean.

2.2 Toy Model

2.2.1 Model Description

We employ the one-dimensional coupled ocean–ice–atmosphere column model developed by Hankel et al. (2023), representing Arctic conditions at 80°N. The model resolves the coupled evolution of sea ice thermodynamics and atmospheric processes within a highly simplified framework. The system includes eight prognostic variables: ocean mixed layer temperature (T_o), sea ice volume (V_{SI}), sea-ice fraction (F_{SI}), sea ice surface temperature (T_{SI}), atmospheric boundary layer temperature (T_B), boundary layer specific humidity (Q_B), tropospheric temperature (T_A), and tropospheric specific humidity (Q_A). The model represents a single grid cell (1 km $\times$ 1 km) and accounts for radiative, turbulent, and thermodynamic exchanges between the ocean, sea ice, and atmosphere. A schematic representation of the model structure and its main variables is shown in fig. 2.1. In Hankel et al. (2023), the model was primarily used to investigate Arctic sea ice bistability under different CO_2 forcing and initial conditions. In the present study, we instead use the model as a process-based framework to interpret differences in Arctic warming across GCMs. To this end, the model is initialized and parameterized using quantities derived from the analyzed GCM simulations.

2.2.2 Governing Equations

The model describes the coupled evolution of ocean, sea ice, and atmosphere within a vertically integrated column, accounting for radiative, convective, and thermodynamic exchanges. Here we summarize some of the equations governing key processes.

The evolution of ocean mixed layer temperature is given by:

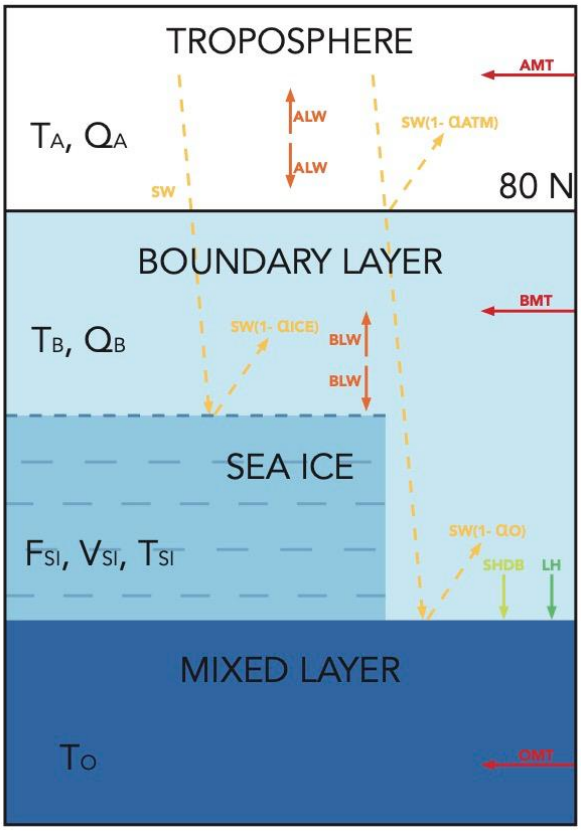

Figure 2.1: Schematic representation of the toy model structure and its main variables. T_A, T_B, T_{SI} and T_O denote the temperatures of the troposphere, boundary layer, sea ice, and ocean mixed layer, respectively. Q_A and Q_B represent the specific humidity of the troposphere and boundary layer. F_{SI} and V_{SI} denote sea ice fraction and volume. SW represents shortwave radiation fluxes; ALW and BLW denote longwave radiation from the troposphere and boundary layer. AMT, BMT and OMT represent atmospheric, boundary layer, and oceanic meridional transport, while SH and LH indicate sensible and latent heat fluxes.

$$\frac{dT_o}{dt} = \frac{1}{D}\frac{1}{\rho_o c_p^{\text{water}}}(1-F_{SI})\Big[SW(y)(1-\alpha_{\text{atm}})(1-\alpha_o) - \sigma T_o^4 + \\ - C_w \nu_H L_e \rho_{\text{air}}(q_s(T_o) - Q_B) - (T_o - T_B)C + \varepsilon\sigma T_a^4\Big] + F_{IO} + \frac{T_{\text{mid},o} - T_o}{\tau_o} \tag{2.3}$$

The first term represent the exchanges over open water between air and ocean, including: shortwave radiation directly absorbed by the open ocean (SW), longwave emission, turbulent

latent and sensible heat fluxes, and atmospheric longwave forcing. The second term F_{IO} accounts for the heat exchange between ocean and ice. The third term parametrizes horizontal oceanic heat transport from midlatitudes, as a relaxation equation towards prescribed midlatitude temperatures. The ocean is represented as a black body the atmosphere shows a specific emissivity ε. Atmospheric emissivity is parametrized as:

$$\varepsilon = \varepsilon_0 + 0.041 \times \log_2(\mathrm{CO_2}/280\mathrm{ppm}) + 0.072 \times \max(0, \log(Q_A/q_0)) + \Delta\varepsilon_{cld} \tag{2.4}$$

Where ε_0 is the clear-sky emissivity without CO_2 and H_2O. Emissivity of atmosphere is a function of CO_2, water vapour concentration, and longwave forcing due to convective clouds. $\Delta\varepsilon_{cld}$ is the effect of high convective clouds on LW emissivity and it is a function of the convective moisture flux ($\Delta\varepsilon_{cld}$).

The heat flux between ocean and ice is defined as:

$$F_{IO} = \begin{cases} -\dfrac{T_o - T_f}{\tau_f} & T_o < T_f \\ -\dfrac{F_{SI} \cdot (T_o - T_f)}{\tau_f} & \text{otherwise} \end{cases} \tag{2.5}$$

The total heat flux through the ice (F_{sfc}) depends on solar radiation absorbed by the ice, depending on atmospheric and ice albedo (α_{ice} and α_{atm}) , the LW radiation from the atmosphere, the upward radiative cooling by LW radiation from the surface, and the sensible heat between sea ice surface and boundary layer.

$$F_{sfc} = SW(y)(1-\alpha_{atm})(1-\alpha_{ice}) + \sigma\varepsilon T_a^4 - \sigma T^4 - (T_{SI} - T_B)C \tag{2.6}$$

Two regimes are distinguished. When surface melting occurs ($T_{SI} \geq 0$ and $F_{sfc} \geq 0$), all excess energy contributes to ice melt and the surface temperature remains at the melting point:

$$\begin{aligned} \frac{dV}{dt} = \big(c_p^{\mathrm{water}} \rho_{\mathrm{water}} D \Delta x \Delta y F_{IO} - A_{\mathrm{ice}} \big[& SW(y)(1-\alpha_{\mathrm{atm}})(1-\alpha_{\mathrm{mp}}) \\ & + \sigma\varepsilon T_a^4 - \sigma T^4 + (T_B - T_{SI})C \big] \big) \frac{1}{L_f \rho_{\mathrm{ice}}} \end{aligned} \tag{2.7}$$

And

$$\frac{dT_{SI}}{dt} = 0 \tag{2.8}$$

The rate of change of the sea ice volume depends on the heat budget and radiative budget at the bottom and upper surface of the sea ice, respectively the ice-ocean and ice-atmospheric exchanges. Otherwise ice growth and surface temperature evolution are governed by basal heat flux and conductive heat transfer through the ice:

$$\frac{dV}{dt} = (c_p^{water}\rho_{water}D\Delta x\Delta y F_{IO} - A_{ice}\frac{c_p^{ice}\rho_{ice}\kappa(T_{SI}-T_f)}{H_{ice}})\frac{1}{L_f\rho_{ice}} \tag{2.9}$$

$$\frac{dT_{\mathrm{SI}}}{dt} = \big(\frac{-c_p^{ice}\rho_{ice}\kappa(T_{\mathrm{SI}}-T_f)}{H_{ice}} + F_{sfc}\big)\frac{1}{h_{sfc}c_p^{ice}\rho_{ice}} \tag{2.10}$$

Where H_{ice} is the ice thickness and $\mathrm{h}_{sfc} = 10$ cm is the depth of ice near the surface.

The rate of change of the temperature of the surface atmospheric boundary layer (T_b) is a function of boundary layer-ocean and boundary layer-ice sensible heat fluxes, latent heat from condensing precipitation (where P_b is the precipitation rate in boundary layer), a convective heat flux, heat flux from the midlatitudes, and a term of subsidence (S):

$$\frac{dT_B}{dt} = \frac{g}{\Delta p_{BL}c_p^{air}}[(1-F_{SI})(T_o-T_B)C + F_{SI}(T_{ice}-T_B)C + \rho_{water}L_eP_b] - F_{c,b} + \frac{T_{mid,BL}-T_B}{\tau_a} + S \tag{2.11}$$

Where convection is active when a parcel from the surface is warmer than the air aloft when lifted adiabatically. The convective flux is positive upward. When the boundary layer is cooler than the lifted parcel there is no convection.

$$F_{c,b} = \begin{cases} \dfrac{T_B-\theta_a}{\tau_c} & T_p < T_a \\ 0 & \text{otherwise} \end{cases} \tag{2.12}$$

A change in T_{mid} is defined depending on CO_2 concentration for all the atmospheric layers.

$$\Delta T_{\mathrm{mid}} = \Delta T_{2\times\mathrm{CO}_2}\ln(\frac{\mathrm{CO}_2}{280}) \tag{2.13}$$

$\Delta T_{2\times\mathrm{CO}_2}$ is a parameter giving the increase of temperature from midlatitude per doubling of CO_2.

Boundary layer specific humidity evolves according to:

$$\frac{dQ_B}{dt} = \frac{g}{\Delta p_{BL}}[C_w v_H \rho_{air}(q_s(T_o)-Q_B)(1-F_{SI}) - P_b\rho_{water}] - Q_{c,b} + \frac{q_{mid,BL}-Q_B}{\tau_a} \tag{2.14}$$

it is governed by the evaporation rate and precipitation close to the surface, convective moisture transport upward, and moisture transport from the mid-latitudes. The midlatitude moisture flux above is a function of the midlatitude temperature while assuming fixed relative humidity of midlatitudes ($\mathrm{RH}_{\mathrm{bl}}$) and is given by:

$$q_{\mathrm{mid,bl}} = \mathrm{RH}_{\mathrm{atm}} \times q_{\mathrm{s}}(\mathrm{T}_{\mathrm{mid,bl}}) \tag{2.15}$$

and $q_s(T)$ the saturation specific humidity which follows the Clausius-Clapeyron relation. The precipitation in boundary layer then is parametrized as:

$$P_b = \begin{cases} \frac{1}{\tau_p}\frac{\Delta p_{BL}}{g\rho^{water}}[Q_B - Rq_s(T_B)] & Q_B < Rq_s(T_B) \\ 0 & \text{otherwise} \end{cases} \tag{2.16}$$

The temperature of the tropospheric layer (T_A) is governed by the equation:

$$\frac{dT_A}{dt} = \frac{g}{\Delta p_{\text{ATM}} c_p^{\text{air}}}[\varepsilon(1-F_{SI})\sigma T_o^4 + \varepsilon F_{SI}\sigma T_{SI}^4 + \rho_{\text{water}} L_e P_a - 2\varepsilon\sigma T_A^4] + \frac{\Delta p_{BL}}{\Delta p_{\text{ATM}}} F_{c,a} + \frac{T_{\text{mid,a}} - T_A}{\tau_a} + S \tag{2.17}$$

Where S is a prescribed temperature tendency due to subsidence, $T_{\text{mid,a}}$ is the tropospheric temperature of the midlatitudes, $F_{c,a}$ is a convective heat flux, P_a is the rate of precipitation from the atmospheric layer in meters per second, ε is the emissivity of the atmosphere, given in eq. 2.4. The rate of change of specific humidity of the tropospheric layer Q_A is determined by a moisture flux due to convection, precipitation that removes moisture and a moisture flux from midlatitudes:

$$\frac{dQ_A}{dt} = \frac{\Delta p_{BL}}{\Delta p_{\text{ATM}}} Q_{c,a} - \frac{g}{\Delta p_{\text{ATM}}} P_a \rho_{\text{water}} + \frac{q_{mid,a} - Q_A}{\tau_a} \tag{2.18}$$

The midlatitude moisture flux above is a function of the midlatitude temperature while assuming a fixed relative humidity of the midlatitudes and is given by $q_{mid,a} = \text{RH}_{\text{atm}} \times q_s(T_{mid,a})$ as in the boundary layer.

2.2.3 Numerical Implementation

The toy model is implemented in Python and integrated using the LSODA adaptive ODE solver from the SciPy library. The solver automatically switches between stiff and non-stiff integration schemes, which is required given the strong nonlinearities associated with phase transitions and radiative feedbacks. Numerical convergence issues were encountered at high CO_2 concentrations. To address these instabilities we reverted to an earlier Python/SciPy version (Python 3.7), in which most instability related issues were absent. In addition solver time-step limits and tolerance parameters were adjusted to identify a stable configuration preventing numerical divergence. Simulations are integrated until a steady state is reached. The steady state is defined as the condition in which the daily effective sea ice thickness changes by less than 1 cm between consecutive years and the daily surface temperature differs by less than 0.15 K from the corresponding day of the previous year. Once this convergence criterion is satisfied, the final simulated year is retained to characterize the equilibrated seasonal cycle. The model is provided in Hankel et al. (2023) with a default parameter configuration tuned to reproduce realistic Arctic seasonal cycles under preindustrial and doubled CO_2 conditions. In this study,

the model is adapted to GCM outputs by modifying a subset of sensitive parameters identified through preliminary sensitivity experiments. These parameters primarily control radiative processes and meridional heat transport. Their values are derived from CMIP6 diagnostics to ensure consistency between the toy model and the GCM simulations. Attempts to directly impose GCM-derived horizontal heat transport as an external forcing led to unstable or unphysical solutions. Instead GCM information is incorporated indirectly through the parameter $\Delta T_{2\times CO_2}$, which controls the strength of the relaxation toward midlatitude temperatures. This approach preserves model stability while retaining information about the magnitude of large scale heat transport across different GCMs. All simulations are initialized from the same initial state and integrated under fixed parameter sets representative of either reference or modern climate conditions of the individual GCM.

2.3 Methods

2.3.1 Arctic Amplification Metrics

Arctic Amplification is quantified using output from the three CMIP6 global climate models GFDL, IPSL, and CMCC. Monthly mean near surface air temperature from all available ensemble members is analyzed for the historical, and idealized 1pctCO_2 experiments. Ensemble means are computed prior to all diagnostics. The Arctic domain is defined as latitudes north of 66°N, while global means are computed over all latitudes. AA is first defined as the difference between Arctic and global near surface temperature anomalies (Linke et al. 2023; Francis et al. 2015):

$$\mathrm{AA}_{\mathrm{difference}} = \Delta T_{\mathrm{S,Arctic}} - \Delta T_{\mathrm{S,global}}, \tag{2.19}$$

where ΔT_{S} denotes monthly mean near surface temperature anomalies. This metric avoids instabilities associated with near zero global anomalies but exhibits relatively high temporal variability (Hind et al. 2016; Davy et al. 2018; Huo et al. 2024). AA is also quantified using a ratio based metric (Ono et al. 2022):

$$\mathrm{AA}_{\mathrm{ratio}} = \frac{\Delta T_{\mathrm{S,Arctic}}}{\Delta T_{\mathrm{S,global}}}, \tag{2.20}$$

which normalizes Arctic warming by the global response but is sensitive to small global anomalies. In addition, a trend based metric is considered:

$$\mathrm{AA}_{\mathrm{trend}} = \frac{|\mathrm{d}T_{\mathrm{Arctic}}/\mathrm{d}t|}{|\mathrm{d}T_{\mathrm{Global}}/\mathrm{d}t|}, \tag{2.21}$$

where linear trends are computed for each calendar month using ordinary least squares regression applied to spatially averaged near surface temperature time series. This metric highlights differences in warming rates and is more robust on multidecadal timescales (Johannessen et al.

2016; Huo et al. 2024). AA is evaluated for the historical and 1pctCO2 experiments within the reference and later periods and corresponding 30 years windos of time defined in section 2.1.2.

2.3.2 Radiative Kernel Method

Climate feedbacks are diagnosed using the radiative kernel linearization (Soden et al. 2008; Shell et al. 2008). Top of atmosphere radiative flux anomalies are approximated as a linear superposition of radiative contributions due to anomalies of relevant state variables. The Feedback processes contributions to the Arctic warming are derived using pre-computed radiative kernels, which quantify the change in the TOA radiative balance due to a 1 K perturbation in atmospheric temperature. In Linke et al. (2023) Article, they employ radiative kernels from the CAM5 (Pendergrass et al. 2017), GFDL-AM2 (Feldl et al. 2017), ERA-Interim (Huang et al. 2017), and HadGEM3-GA7 (Smith et al. 2020) models. For each climate model, the lapse rate feedback (LRF) is calculated individually with each kernel, and the resulting mean kernel represents the model specific LRF. Importantly, the inter-models correlation between AA and LRF is only weakly dependent on the choice of kernel, with correlation coefficients. For this reason we chose one single pre-computed radiative kernel to compute feedbacks warming contribution.

The feedback parameter λ is defined following the radiative kernel formalism as

$$\lambda = \frac{\partial R}{\partial X}\frac{\Delta X}{\Delta T_S}, \tag{2.22}$$

where R is the radiative flux and $\partial R/\partial X$ denotes the radiative kernel (in W m^{-2} K^{-1}), and ΔX represents the deviation of the vertical profile of the variable X given a near surface temperature anomaly ΔT_S. The feedback contribution is obtained by applying Eq. 2.22 and vertically integrating over the troposphere. The feedback parameter λ has units of W m^{-2} K^{-1}.

To express the feedback parameter in terms of its contribution to surface warming,they use the local energy budget approach (Lu et al. 2009; Crook et al. 2011; Feldl et al. 2013; Taylor et al. 2013; Pithan et al. 2014; Goosse et al. 2018; Hahn et al. 2021):

$$0 = F + \left(\sum_i \lambda_i + \overline{\lambda_P} + \lambda_P'\right)\Delta T_S + \Delta\text{OHU} + \Delta\text{AHT} \tag{2.23}$$

where F is the effective radiative forcing (the forcing before the surface temperature has responded), λ_P the Planck feedback, λ_i the individual feedback parameters, ΔOHU the ocean heat uptake anomaly, and ΔAHT the anomalous atmospheric heat transport convergence. The Planck feedback is decomposed into its global mean, $\overline{\lambda_P}$, and its spatial deviation, $\lambda_P' = \lambda_P - \overline{\lambda_P}$. Dividing Eq. 2.23 by $\overline{\lambda_P}$ gives the warming contributions to ΔT_S:

$$\Delta T_S = -\frac{(F + \Delta\text{OHU} + \Delta\text{AHT})}{\overline{\lambda_P}} - \frac{(\lambda_P' + \sum_i \lambda_i)\Delta T_S}{\overline{\lambda_P}} \tag{2.24}$$

In this form, each term on the right hand side represents a distinct energetic contribution to the total near surface temperature change. In Linke et al. (2023) analysis they isolate the contribution of the lapse rate feedback to ΔT_S (main focus of the study).

To evaluate the strength of feedback processes in the 3 different GCMs we use the radiative kernels validated and calculated with the large ensemble version of CAM5, CESM1.1.2 by Pendergrass et al. (Pendergrass et al. 2017), at the top of the atmosphere and at the surface. In the arcticle estimates of the radiative forcing from greenhouse gases and aerosols in RCP8.5 in the CESM large ensemble simulations are also diagnosed. As an application, feedbacks are calculated for the CESM large ensemble. The kernels are available at Pendergrass (2017a), and accompanying software has been downloaded from Pendergrass (2017b). A demo of the radiative kernel matlab software given by Pendergrass et al. has been run and data for this reseatch have been adapted to be processed by the pre-computed radiative kernel. A brief explanation of dataset preparation is shown in the appendix 5.

Warming Contributions of Individual Processes in GCMs

Once the datasets based on IPSL, GFDL and CMCC outputs are constructed, the precomputed radiative kernels are applied to these datasets. For each of the GCMs analyzed, three distinct regions are selected in order to compute the feedback parameters associated with individual feedback processes. Specifically, we consider the Arctic, tropical, and global regions. To isolate these regions, a latitude based mask is applied:

- Arctic region: $66°N - 90°N$
- Tropical region: $30°S - 30°N$
- Global region: $90°S - 90°N$

The feedback processes analyzed using the radiative kernels include water vapor feedback (WVF), surface albedo feedback (SAF), Planck feedback (Planck), lapse rate feedback, temperature feedback (Planck + lapse rate, TF), and both shortwave (SWCF) and longwave (LWCF) cloud feedbacks. For each process, the feedback parameter λ_i defined in sec. 2.3.2 is computed for each region and for each of the considered GCMs. In addition, a seasonal decomposition of the data is performed, and the feedback parameters λ_i are computed separately for boreal winter (DJF) and boreal summer (JJA) for each model and region.

To quantify the contributions of individual processes to near surface temperature warming (ΔT_S), we reinterpret the feedback parameters in terms of temperature contributions using the local energy budget framework, following several previous studies (Linke et al. 2023; Feldl et al. 2013; Taylor et al. 2013; Pithan et al. 2014; Goosse et al. 2018; Hahn et al. 2021). The local energy budget can be written as in Eq. 2.23, and it describes the energetic contributions of the radiative forcing F , the feedbacks (($\lambda_i \Delta T_S$), and the Planck response ($\lambda_P \Delta T_S$), as well as the ocean heat uptake (ΔOHU) and the anomalous atmospheric heat transport convergence

(ΔAHT). The second step splits the Planck feedback into its global mean value, $\overline{\lambda_P}$, and the spatially resolved deviation from it, $\lambda'_P = \lambda_P - \overline{\lambda_P}$. Therefore, we can derive the warming contributions to ΔT_S from the forcings and feedbacks by computing each term in Eq. 2.24. We computed the OHU and AHT terms directly from each GCMs dataset, using the energy budget equation and obtaining the horizontal heat transport and ocean heat uptake for all the above regions. The result is in W/m^2, to convert them in processes warming contributions in K, for each region it becomes:

$$\Delta\text{AHT} = \frac{\langle \text{AHT} \rangle}{2\pi R_T^2 (\sin\phi_2 - \sin\phi_1)} \tag{2.25}$$

Where ϕ_1 and ϕ_2 are the latitudes delimitating the region, R_T the radius of the Earth and $\langle \text{AHT} \rangle$ the time and space average AHT for the selected region and period. The same equation is used to compute ocean heat uptake warming contribution in K.

Each of the individual contributions on the right hand side in Eq. 2.24 add up to the full change in T_S. In our study, we consider the contribution of the feedbacks and the atmospheric heat transport anomaly and the Ocean Heat Transport anomaly to ΔT_S .

2.3.3 Toy Model Calibration

To ensure consistency with the GCM simulations, the toy model is calibrated by constraining a subset of parameters using CMIP6 models outputs. A preliminary sensitivity analysis is used to identify the parameters that exert the strongest control on the model steady state. These parameters primarily govern radiative processes and the representation of meridional heat transport. This reduced set of sensitive parameters is modified, while all remaining parameters are kept at their default values from Hankel et al. (2023). The list of selected parameters is shown in table 2.1, A complete list of model parameters is provided in the appendix 5.

Heat Transport from Midlatitudes

Heat transport within the toy model prognostic equations is represented as a relaxation equation:

$$\text{Transport} = \frac{T_{\text{mid,i}} - T_{\text{i}}}{\tau_{\text{i}}} \tag{2.26}$$

Where $\Delta T_{\text{mid,i}}$, T_{i} and τ_{i} are respectively midlatitude temperature of the i-th column layer given as an input parameter, the temperature of the i-th column layer and the specific layer time scale. To adapt this term in the prognostic equations and add GCMs-derived informations to the toy model configuration, we computed the mean oceanic and atmospheric horizontal heat transport from 79°N to 81°N. A climatology has been computed for both the reference (1951-1985) and modern (1985-2014) period. The attempt to insert specific horizontal transport to each GCM-adapted simulation as an external forcing within the toy model gave unphysical results. We then characterize the $\Delta T_{\text{mid,i}}$ (2.13) with informations from GCMs. We compute a

new GCM adapted degree per doubling of CO_2 parameter as:

$$\Delta T_{2\times CO_2} = \frac{\Delta \mathrm{AHT}}{\mathrm{AHT}} \frac{T_{\mathrm{mid}}}{\ln(CO_2/280)} \tag{2.27}$$

Where ΔAHT is the atmospheric warming contribution due to transport from GCMs data normalized by Eq. 2.25 and T_{mid} is the default midlatitude temperature given by the article. This way to define $T_{\mathrm{mid,i}}$ doesn't give quantitatively the same transport in toy model as in GCMs, but it contains information on the qualitative strength and the rate of change of horizontal transport in different GCMs frameworks. The toy model results too sensitive to oceanic transport modifications, for this reason the $T_{\mathrm{mid,o}}$ parameter has been kept the default one for all the GCMs adapted simulations.

Radiative Diagnostics

In order to quantify the role of radiative processes in the Arctic region, a set of albedo and effective emissivity diagnostics was computed from CMIP6 monthly mean radiative fluxes. All diagnostics are evaluated averaging between 79° to 81° N (to adapt the variable to the simple model) and are subsequently averaged spatially over latitude and longitude and temporally into monthly climatologies.

Radiative variables are taken from the CMIP6 Amon frequency and include upwelling and downwelling shortwave and longwave fluxes under both all-sky and clear-sky conditions, as well as near surface air temperature. For each model and experiment, ensemble mean is computed on al the ensemble members. The specific calculation are shown in the appendix 2.3.3. We defined for each GCM two sets of parameters using average dataset from reference and modern period in the historical experiment.

The list of toy model sensitive parameters changed with GCM derived parameters is shown in tab. 2.1. A list complete of toy model parameters is shown in the appendix 5.

Category	Toy model parameter	GCM variable
Surface	α_{mp}: Albedo of melt ponds α_{ice}: Albedo of bare ice α_o: Ocean surface albedo	α_{sfc}: Surface albedo (all-sky)
Ocean	D: Slab ocean depth	thetao: Mean mixed-layer depth averaged from 79° to 81° N
Atmosphere	$T_{\mathrm{mid,bl}}$: Midlatitude boundary layer reference temperature	$\Delta T_{2\times \mathrm{CO_2}} = \frac{\Delta \mathrm{AHT}}{\mathrm{AHT}} \frac{T_{\mathrm{mid,\,bl}}}{\ln(\mathrm{CO_2}/280)}$, AHT vertically averaged from 1000 to 850 hPa
	$T_{\mathrm{mid,a}}$: Midlatitude tropospheric reference temperature	$\Delta T_{2\times \mathrm{CO_2}} = \frac{\Delta \mathrm{AHT}}{\mathrm{AHT}} \frac{T_{\mathrm{mid,\,a}}}{\ln(\mathrm{CO_2}/280)}$, AHT vertically averaged from 850 to 300 hPa
	ε_0: Clear-sky emissivity without CO_2 and H_2O	$\varepsilon^{\mathrm{cs}}$: Clear-sky effective emissivity
	α_{cld}: Albedo of low clouds	$\alpha_{\mathrm{TOA}} - \alpha_{\mathrm{TOA}}^{\mathrm{cs}}$: TOA albedo difference between all-sky and clear-sky conditions
	$\Delta\varepsilon_0$: Maximum emissivity change due to clouds	$\varepsilon - \varepsilon^{\mathrm{cs}}$: Effective emissivity difference between all-sky and clear-sky
	CO_2: CO_2 concentration in ppm	mean CO_2 concentration in ppm

Table 2.1: List of toy model parameters constrained using diagnostics from CMIP6 simulations. The left column shows the toy model parameters, while the right column shows the corresponding radiative variables from CMIP6 models.

2.3.4 Model Comparison

Seasonal Cycle Comparison

Monthly climatologies are constructed for each model (IPSL, GFDL, and CMCC) over two periods: reference (1951–1980) and modern period(1985–2014), averaging data within the latitude band 79°N and 81°N. For the 1pctCO2 experiment two 30 years windows ($\pm$15 years) centred on the years corresponding to the mean CO_2 concentration of the reference and modern periods are selected. An analogus dataset is created from ERA5 reanalyses, to provide an observational benchmark. Monthly climatologies of 2m-temperature and ice cover are computed for both reference and modern period, over the same latitude band. To assess the ability of the toy model to reproduces the seasonal response to Arctic warming, we compare the seasonal cycles of sea ice fraction, near surface temperature and boundary layer specific humidity between GCM outputs and GCM- adapted toy model simulations. the responses are defined as:

$$\Delta X = X_{\mathrm{modern}} - X_{\mathrm{reference}}, \tag{2.28}$$

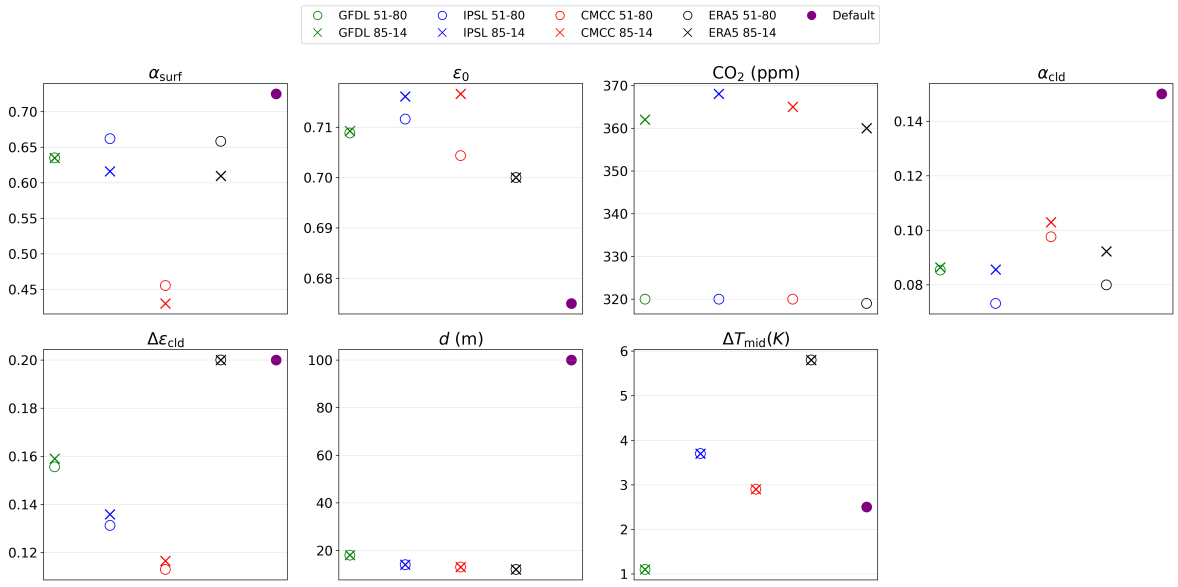

Figure 2.2: Scatter plot of initializations parameters for every model adapted initialization. Green, parameters from GFDL, in blue red abd black, respectively parameters from IPSL, CMCC and ERA5 outputs. In purple the default parameters given in Hankel et al. (2023) article.

where X denotes the monthly value of a given variable. This formulation isolates the seasonal structure of the climate response. To quantify the agreement between the toy model and the GCMs, two complementary metrics are computed for the monthly warming signals. The Pearson correlation coefficient (r), which measures the similarity in the shape and phase of the seasonal response, indicating whether the toy model captures the timing of the GCM warming throughout the year. The normalized root mean square error (nRMSE) which measures the amplitude mismatch of the seasonal response, normalized by the standard deviation of the GCM signal (ΔX), and therefore provides a dimensionless estimate of the relative error. Both metrics were computed separately for each variable and each GCM.

Mechanism Denial Experiments

The role of individual physical processes is investigated through a set of mechanism denial experiments, in which specific feedbacks are selectively suppressed in the modern set of parameters simulations.

To quantify the response of the toy model to each suppressed process, we calculate the difference between boundary layer temperature and sea ice seasonal cycles of the denied process simulations and the modern adapted ones with all processes and we compute the annual mean response:

$$\langle \Delta X_{\text{fb}} \rangle = \langle X_{\text{all-fb}} - X_{\text{no-fb}} \rangle \tag{2.29}$$

Where $X_{\text{all-fb}}$ and $X_{\text{no-fb}}$ are respectively the average monthly prognostic variable of the simple model output within a modern historical period adapted set of initializing parameters and a simulation with the same set of parameters and one suppressed specific process at the time.

The analysis focuses on near surface temperature and sea ice fraction, which provide a direct measure of the thermodynamic and cryospheric response to climate forcing.

The sign of the response indicates the nature of the feedback:

- $\Delta T_{\text{surf}} > 0$: the process acts as a positive feedback (its removal reduces warming)
- $\Delta T_{\text{surf}} < 0$: the process acts as a negative feedback
- $\Delta F > 0$: the process acts as a negative feedback (enhances ice retention)
- $\Delta F < 0$: the process acts as a positive feedback (promotes ice loss)

The mechanisms denial experiments performed are summarized in table 2.2.

Name	Denial Experiment	Description
WV	Clear-sky water vapor feedback suppression	The term in the atmospheric emissivity equation 2.4 that depends on specific humidity is removed, preventing water vapor from affecting longwave radiation.
CC	Convective cloud feedback suppression	The effect of convection on atmospheric emissivity is disabled by setting $\Delta\varepsilon_{\text{cld}} = 0$ in Eq. 2.4.
LR	Lapse rate feedback	Atmospheric emissivity retains its full formulation (CO_2, clouds, and water vapor), but the boundary layer temperature (T_{BL}) used to compute longwave radiation is fixed to its reference seasonal climatology.
SAF	Surface albedo feedback suppression	Surface albedo values (for ice, melt ponds, and ocean) are fixed at reference albedo to represent the Arctic climate as the ice concentration doesn't change from the reference historical period.
AET	Horizontal transport suppression	Horizontal atmospheric and oceanic heat transports are fixed, T_{mid} is fixed to the default value, this affects eq. 2.14, 2.11, 2.3and the evolution of atmospheric temperature and specific humidity relaxation term.

Table 2.2: Summary of mechanism denial experiments used to isolate individual feedback processes in the toy model.

Chapter 3

Results

3.1 General Circulation Models Resutls

3.1.1 Degree of Arctic Amplification and Arctic Warming

Model	Historical		1pctCO2	
	Arctic warming (K)	Global warming (K)	Arctic warming (K)	Global warming (K)
ERA5	1.60	0.66	–	–
CMCC	2.02	0.84	1.16	0.36
IPSL	1.81	0.68	0.61	0.37
GFDL	0.69	0.44	0.37	0.28

Table 3.1: Near surface warming (K) in the Arctic and globally for historical and 1pctCO2 experiments for each model and ERA5 reanalysis data. Warming computed between reference (1951-1980) and modern (1985-2014) climatologies.

Figure 3.1 shows the seasonal cycle of Arctic Amplification computed using the difference based metrics defined in section 2.3. Shading for the historical experiment represents the standard deviation of monthly mean AA across all models and realizations, while no intra-model variability is found for the 1pctCO2 experiment. AA exhibits a clear seasonal cycle, with maximum values in winter and minimum values in summer. Both inter-model and intra-model spread are larger during the cold season. During the warm season, AA approaches zero when using the difference based metric. In the historical experiment, IPSL shows the highest Arctic amplification when using normalized metrics, while CMCC exhibits the largest amplification in absolute terms (difference based metric). The ranking of models depends on the definition of Arctic amplification. CMCC simulates stronger warming both globally

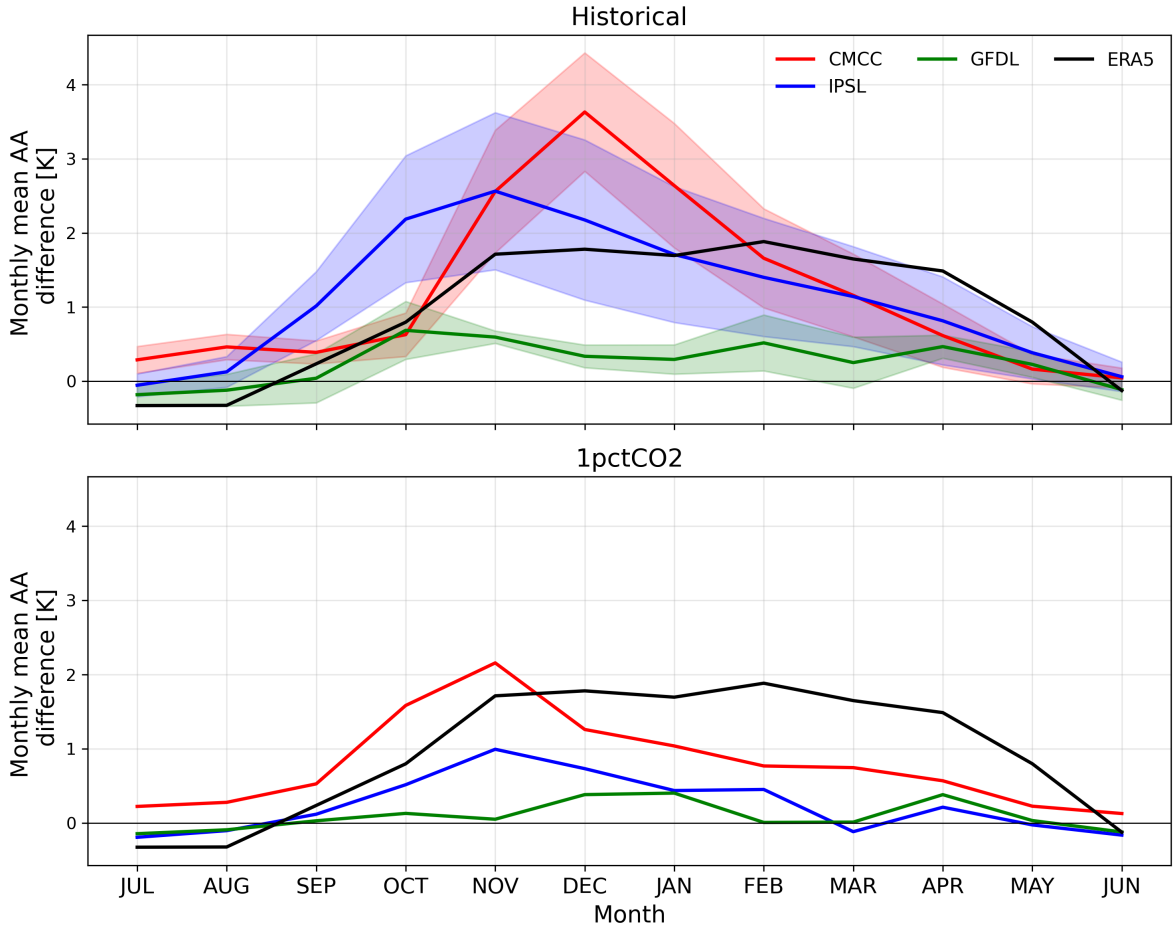

Figure 3.1: Seasonal cycle of Arctic Amplification degree for CMCC-CM2-SR5 (red), GFDL-ESM4 (green) and IPSL-CM6A-LR (blue) data in historical (top plot) and 1pctCO2 (bottom plot) experiments. The AA degree is computed for three different metrics, here is represented the seasonal cycle of difference based one. The shading in the top panel represents the standard deviation across individual model realizations.

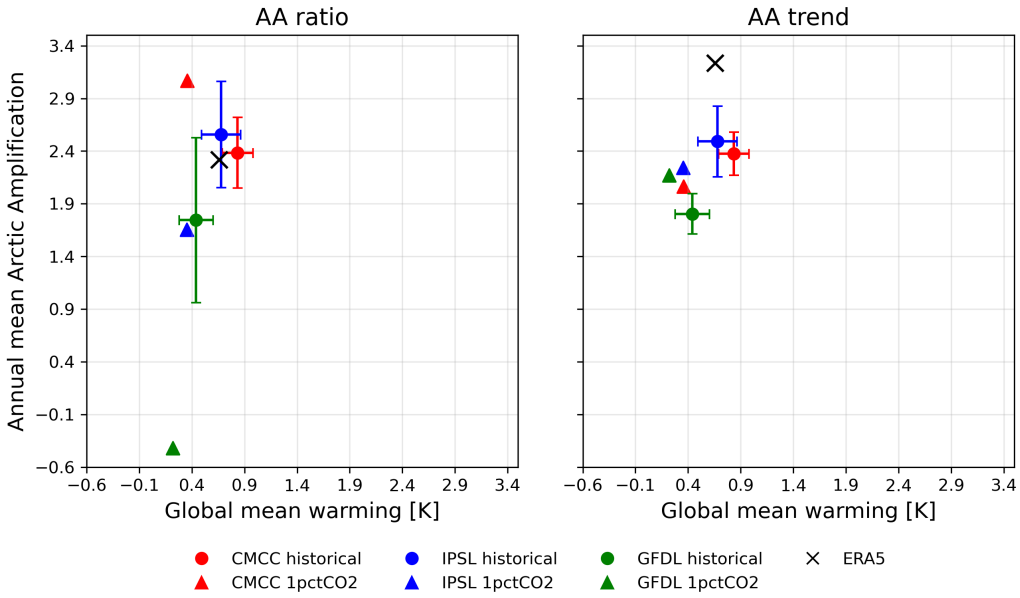

Figure 3.2: Annual mean Arctic Amplification degree for ERA5 reanalysis data (black), CMCC-CM2-SR5 (red), GFDL-ESM4 (green) and IPSL-CM6A-LR (blue) compared with models annual global warming. Triangles and circles represent respectively 1pctCO2 and historical experiments data. Arctic amplification degree is computed with a ratio based metric (left) and with a trend-based metric (right).

	Ratio based AA		**Trend based AA**		**Difference based AA (K)**	
Model	Hist	1pctCO2	Hist	1pctCO2	Hist	1pctCO2
ERA5	2.32	–	3.24	–	0.94	–
IPSL	2.56 ± 0.50	1.66	2.49 ± 0.33	2.24	1.13 ± 0.56	0.24
CMCC	2.38 ± 0.34	3.07	2.38 ± 0.20	2.06	1.19 ± 0.41	0.79
GFDL	1.74 ± 0.78	-0.48	1.80 ± 0.19	2.17	0.25 ± 0.20	0.09

Table 3.2: Annual mean Arctic Amplification degree computed by three different metrics for the three CMIP6 models considered. AA is shown using three different definitions: difference based ($\Delta T_{\text{Arctic}} - \Delta T_{\text{Global}}$), ratio based ($\Delta T_{\text{Arctic}} / \Delta T_{\text{Global}}$), and trend based (ratio of Arctic to global SAT trends). difference based AA is shown in Kelvin.

and in the Arctic, whereas IPSL shows enhanced Arctic warming relative to a more moderate global warming, leading to higher AA in normalized metrics. In the 1pctCO2 experiment the highest AA is simulated by CMCC, which shows a marked deviation from the other models. Overall, IPSL and CMCC simulate slightly stronger difference based AA than ERA5. IPSL reproduces global warming comparable to observations but with enhanced Arctic warming, whereas CMCC simulates stronger warming both globally and in the Arctic. In contrast, GFDL underestimates AA throughout the year. These results are consistent with Linke et al. (2023).

Figure 3.2 presents the annual mean AA as a function of global mean warming using ratio based and trend based metrics. Error bars indicate the standard deviation across realizations. AA is generally stronger in the historical experiment than in the 1pctCO2 experiment at comparable CO_2 levels, suggesting that additional forcings such as aerosols and non-CO_2 greenhouse gases, enhance Arctic warming rather than suppress it, particularly in winter when aerosol albedo effects are limited. For normalized metrics (ratio and trend), the historical experiment shows larger AA in IPSL despite its lower global warming compared to CMCC. Conversely, in the 1pctCO2 experiment, CMCC exhibits higher AA despite similar global warming to IPSL.

Intra-model spread mainly affects AA rather than global warming, indicating that differences in Arctic processes are a primary source of variability across models and realizations. No spread is shown for the 1pctCO2 experiment due to the absence of intra-model variability. In the historical experiment, CMCC shows approximately 0.15 K higher global warming than IPSL, which reduces AA in normalized metrics and compensates for its stronger Arctic warming. According to the ratio based metric, CMCC best reproduces ERA5 AA, despite overestimating global warming, while IPSL reproduces global warming more accurately but overestimates AA. GFDL underestimates both global warming and AA compared to ERA5.

The intra-model spread is reduced in the trend based metric, consistent with its suitability for multi-decadal analysis (Huo et al. 2024). ERA5 exhibits the strongest AA in the trend based metric, indicating a faster Arctic warming rate than in the models, despite comparable trend in global warming. These discrepancies are reflected in the seasonal cycles of near surface temperature and sea ice fraction (fig. 3.3). IPSL reproduces the temperature seasonal cycle well (r= 0.88, nRMSE = 0.68), but shows inconsistencies in simulating sea ice fraction. CMCC produces the warmest Arctic conditions, with nearly ice-free summers, deviating from ERA5 while still reproducing similar AA. GFDL shows limited differences between reference and warm periods, with colder temperatures and weak sea ice changes compared to ERA5.

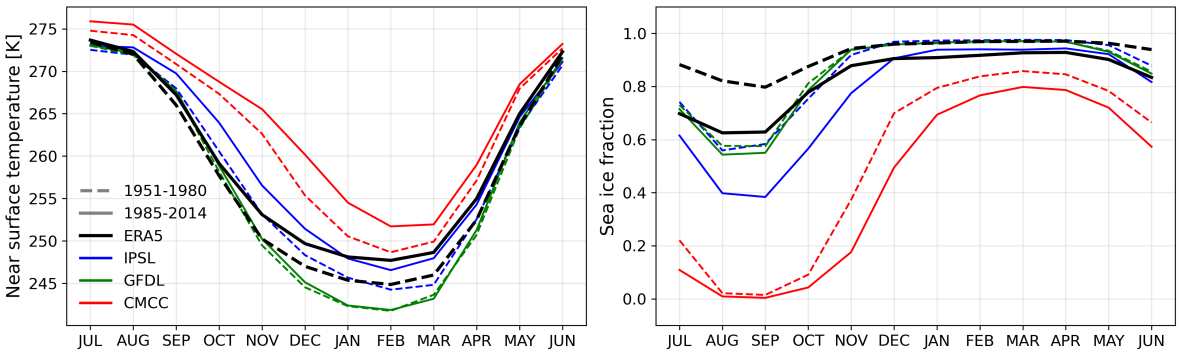

Figure 3.3: Climatology of the seasonal cycle of near surface air temperature and sea ice fraction for the reference (1951-1980) period (dashed lines) and the modern (1985-2014) period (solid lines). ERA5 reanalysis data (black) are compared with the three GCMs: IPSL-CM6A-LR, GFDL-ESM4 and CMCC-CM2-SR5. Data are compared for the historical experiment, showing both reference (dashed lines) and modern (solid lines) climatologies. GCM and ERA5 data are averaged over the latitude band from 79°N to 81° N.

3.1.2 Feedback and Heat Transport Contributions to Arctic Warming in GCMs

This section shows the main results of the analysis of the warming contributions of individual feedback processes. For this section the Pendergrass et al. (2017) pre-computed radiative kernel has been used. A comparison is shown between the warming contributions in the Arctic and the Tropics, normalized by the global Planck feedback for the IPSL, CMCC, and GFDL models. A seasonal analysis of the warming contributions in the Arctic is then presented, specifically separating summer and winter seasons.

Arctic and Tropics Radiative Kernel Based Feedback Analysis

Figure 3.4 shows the annual mean warming contributions of individual feedback mechanisms in the three analyzed GCMs. Tropical warming is shown on the x-axis and Arctic warming on the y-axis. Feedback contributions are computed using the radiative kernel method based on Pendergrass et al. (2017) (see section 2.3). Feedbacks located above the bisector enhance Arctic amplification, while those below oppose it. In the IPSL and CMCC models (CMIP6/s group), the dominant contributor to AA is the surface albedo feedback , followed by the lapse rate feedback . In absolute terms, SAF contributes more strongly to Arctic warming. However, LRF also suppresses tropical warming, thereby enhancing AA relative to the bisector. Previous studies have identified LRF as a key driver of polar amplification due to its contrasting behavior between high and low latitudes (Lu et al. 2009; Bintanja et al. 2011; Pithan et al. 2014). The relative importance of SAF and LRF remains debated .Graversen et al. (2014)

Variable	Model compared to ERA5	r	nRMSE
T_{surf}	IPSL	0.88	0.68
	GFDL	0.11	1.79
	CMCC	0.77	0.68
F_{SI}	IPSL	0.73	0.70
	GFDL	0.86	1.74
	CMCC	-0.39	1.62

Table 3.3: Correlation coefficient (r) and normalized RMSE between ERA5 and different GCMs for near surface temperature and sea ice fraction. The metrics are computed from the monthly differences between the warm state (1985–2014) and the cold state (1951–1980). Statistics refer to the data shown in fig. 3.3

showed that these feedbacks strongly interact at high latitudes and cannot be considered independent at the global scale. The physical mechanisms underlying LRF are moreover less well understood than those governing SAF (Feldl et al. 2020; Boeke et al. 2021; Lauer et al. 2020). In contrast, the GFDL model (CMIP6/w group) shows LRF as the primary contributor to AA, while SAF is negligible. Despite this, the overall AA in GFDL is weak across all metrics (section 3.1.1). This reduced AA appears linked to the absence of a strong SAF, highlighting its role in amplifying Arctic warming. LRF alone is however sufficient to produce a positive, even if weaker, AA. Water vapor feedback , shortwave cloud feedback, and longwave cloud feedback lie close to the bisector, indicating similar contributions to tropical and Arctic warming, particularly in CMIP6/s models. In GFDL, WVF and LWCF instead favor stronger tropical warming, thereby opposing AA. The combination of enhanced tropical warming from longwave related feedbacks and weak SAF leads to reduced AA in this model. Most inter-model differences project onto the Arctic, indicating that discrepancies primarily arise from the representation of Arctic feedback processes. In contrast, tropical warming contributions show relatively minor differences across models. Contributions from horizontal oceanic and atmospheric heat transport anomalies are negligible in this framework. This likely reflects the use of large spatial domains and annual means, which may mask compensating regional and seasonal effects. A more detailed seasonal and regional analysis could better constrain their role in polar warming. The relative importance of SAF and LRF is generally consistent with Pithan et al. (2014). Differences with previous studies arise from the use of individual models rather than multi-model means, as well as from methodological differences in the treatment of the Planck feedback.

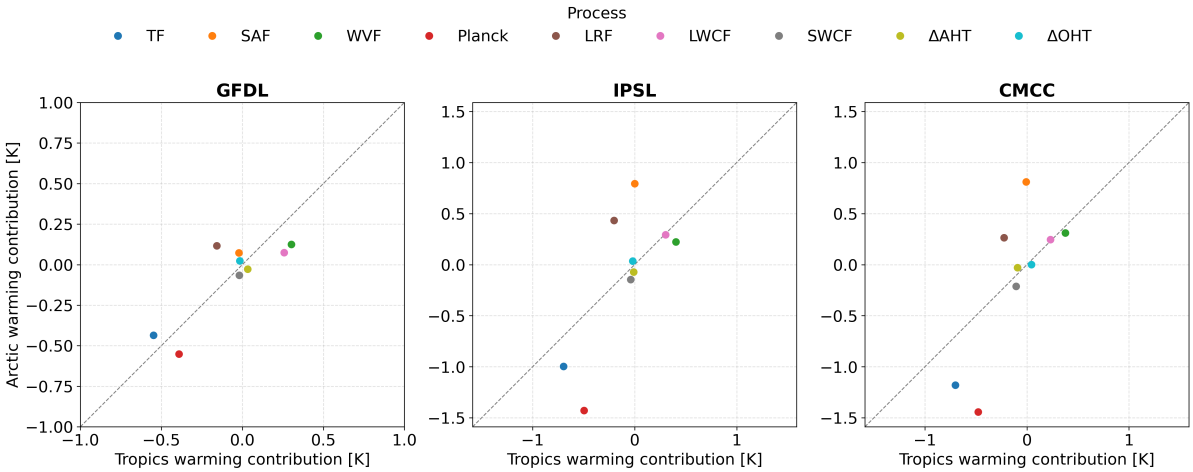

Figure 3.4: Annual average warming contributions of individual feedback mechanisms of IPSL-CM6A-LR, CMCC-CM2-SR5 and GFDL-ESM4 models. The figure shows the Arctic versus tropical near-surface temperature warming. Feedbacks above the bisector line contribute to Arctic amplification, whereas feedbacks below the line oppose Arctic amplification. OHT includes the effect of ocean transport changes and ocean heat uptake.

Seasonal Radiative Kernel Based Arctic Feedbacks Analysis

Figure 3.5 shows the seasonal mean warming contributions from individual feedbacks and horizontal oceanic and atmospheric heat transport changes in the IPSL, CMCC, and GFDL models. Contributions are computed using the radiative kernel method of Pendergrass et al. (2017), considering winter (DJF) and summer (JJA) separately, and are normalized by the seasonal global Planck feedback. Given that Arctic warming peaks in winter, analyzing the seasonal structure of feedbacks and transport anomalies is significant. The results show that the dominant wintertime contribution arises from the lapse rate feedback, which reaches about 1.2 K in CMCC and 0.9 K in IPSL, and is much weaker in GFDL. This makes LRF the primary source of inter-model spread during winter. Other feedbacks, including surface albedo, water vapor, and cloud feedbacks, contribute positively in CMCC and IPSL during winter (around 0.4 K and 0.2 K, respectively), but are negligible in GFDL. In particular, SAF becomes slightly negative in GFDL, consistent with increased winter sea ice, which suppresses its warming effect. Although SAF is not directly active in winter due to the absence of solar radiation, clear inter-model differences in feedback strength persist, with CMCC showing the strongest contributions, followed by IPSL and then GFDL. In summer the largest inter-model difference is associated with SAF, which reaches about 0.75 K in CMCC and IPSL but remains much smaller in GFDL (around 0.1K). WVF shows a similar ranking as in winter, with reduced magnitude. Cloud feedbacks exhibit the largest discrepancies: LWCF is weakly positive in IPSL and GFDL but slightly negative in CMCC, while SWCF is strongly positive in CMCC

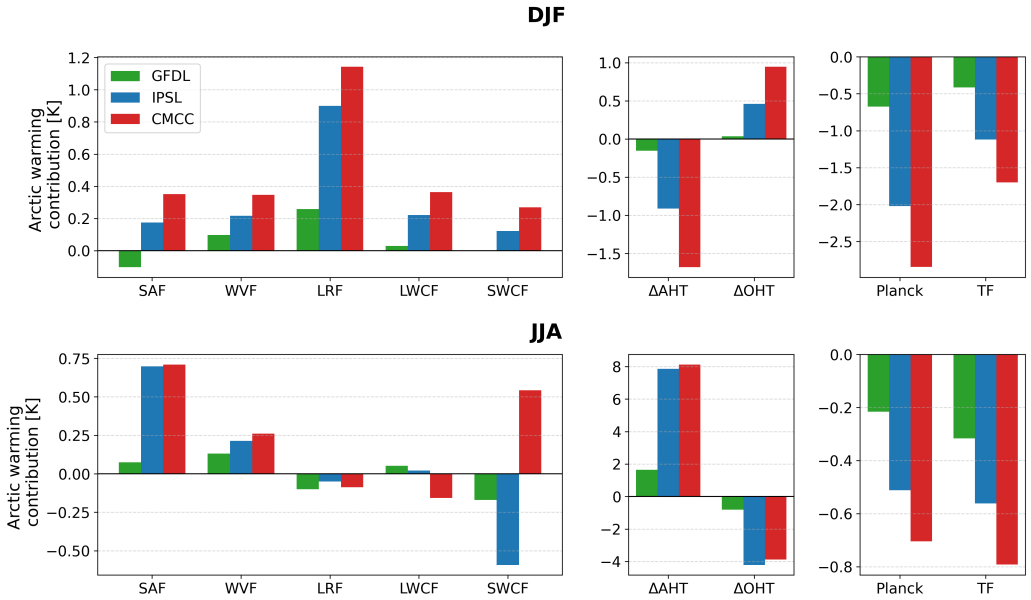

Figure 3.5: Seasonal average warming contributions of individual feedback mechanisms and horizontal transport of IPSL-CM6A-LR (blue) CMCC-CM2-SR5 (red) and GFDL-ESM4 (green) models. The figure shows the Arctic winter (DJF) and summer (JJA) near-surface temperature warming for individual feedback processes. All the warming contributions are normalized with global mean Planck feedback. Different boxes have been showed to highlight different scales.

(about 0.5 K), strongly negative in IPSL (about -0.5 K), and weakly negative in GFDL. This confirms that cloud feedbacks are still a source of uncertainty in Arctic warming (Eastman et al. 2010; Ridley et al. 2016; Sledd et al. 2023). Atmospheric (ΔAHT) and oceanic (ΔOHT) heat transport anomalies show strong seasonal compensation. In winter, ΔAHT contributes negatively, while ΔOHT contributes positively. In summer, ΔAHT becomes the dominant warming contribution (up to $\sim$8 K in CMCC and IPSL), whereas ΔOHT is strongly negative (around -4 K). Despite their large seasonal amplitudes, their annual mean contribution is close to zero. The large summer ΔAHT and SAF contributions may induce delayed effects that enhance winter Arctic warming. Energy absorbed by the ocean during summer can be released in winter, amplifying near surface warming and sea ice loss (Serreze et al. 2011; Stroeve et al. 2014; Carvalho et al. 2020; Zhang et al. 2023). The Planck feedback is strongly negative in winter, partially offsetting positive feedbacks, and remains negative but weaker in summer. This seasonal contrast reflects differences in radiative damping and the response timescales of the climate system.

The largest inter-model differences between CMIP6/s models and GFDL arise from LRF and Planck feedback in winter, and from SAF and ΔAHT in summer. LRF is the dominant winter feedback, while ΔAHT provides the largest absolute summer contribution. Transport effects largely cancel over the annual cycle, but their seasonal imbalance, together with SAF, may contribute to delayed Arctic warming and the winter maximum of Arctic amplification. Cloud feedbacks, particularly SWCF, remain an important source of uncertainty and inter-model spread. Across most processes, CMCC shows the strongest contributions, followed by IPSL and GFDL.

3.2 Toy Model Results

In this section we present the main results of the toy model simulations and evaluate their ability to reproduce key features of Arctic climate variability. The analysis first compares the model output with ERA5 reanalysis data to assess how well the toy model represents observed seasonal cycles of near surface temperature and sea ice fraction. The model performance is then examined against simulations from three analyzed GCMs. To investigate the inter-model spread the toy model is calibrated separately using parameters derived from each GCM, and the resulting simulations are analyzed to assess whether the toy model can reproduce the differences between the GCMs. Finally, once the toy model is adapted to each GCM configuration, mechanism-denial experiments are analyzed to evaluate the role of individual feedback processes in shaping Arctic warming and sea ice loss across the different simulations.

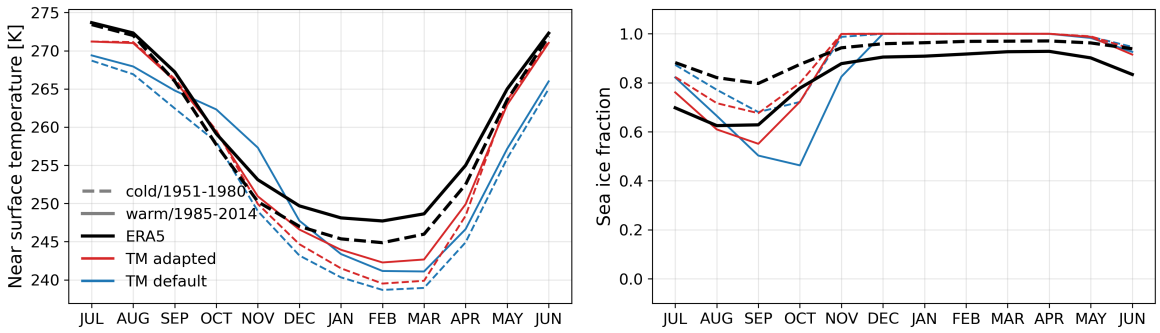

Figure 3.6: Climatological seasonal cycles of near surface temperature and sea ice fraction. For ERA5 (black), solid lines represent the modern/warm period (1985-2014) and dashed lines the reference/cold period (1951-1980). Toy model results correspond to the seasonal cycle of the final simulation year before reaching steady state, with solid lines indicating the warm period and dashed lines the cold period. The toy model is shown for both the default configuration (blue), where only CO_2 is adjusted to match ERA5 climatological values, and an ERA5-adapted configuration (dark red).

Figure 3.6 shows the climatological seasonal cycles of near surface air temperature and sea ice fraction for the periods 1951-1980 and 1985-2014. ERA5 reanalysis data are compared with outputs from the toy model, both in its default configuration and with parameters adapted to ERA5 data. ERA5 data are computed as climatological means over each period and averaged over the latitude band 79°N-81°N. The toy model seasonal cycles correspond to the final simulation year before to reaching steady state. Simulations are performed using the default parameter configuration, with only CO_2 concentration adjusted to match the climatological values of the two periods, the main reason could be the higher mixed layer depth in the default configuration. The ocean therefore acts as a balancer and absorbs more heat, making the tem-

Variable	Compared dataset	r	nRMSE
ΔT_{surf}	TM-adapted	0.83	3.42
	TM-default	0.59	1.90
ΔF_{SI}	TM-adapted	0.89	1.19
	TM-default	0.44	1.52

Table 3.4: Correlation coefficient (r) and normalized RMSE between ERA5 and different model configurations for near surface temperature and sea ice fraction change. The metrics are computed from the monthly differences between the warm state (1985–2014) and the cold state (1951–1980). Statistics refer to the data shown in fig. 3.6

perature near the surface warmer once it equilibrates in a longer time. Additional simulations include an adapted parameter configuration tuned to ERA5. In its default configuration, the toy model underestimates near surface air temperature compared to ERA5 in both periods. Despite this, it simulates a larger sea ice loss, indicating an inconsistent warming response. While the model captures the general shape of the seasonal cycle, it fails to reproduce the observed warming response when only CO_2 is adjusted. After parameter adaptation, the model still underestimates absolute temperatures but more accurately captures the response to a warmer climate in both temperature and sea ice fraction. The correlation with ERA5 improves from r= 0.59 in the default configuration to $r = 0.83$ in the adapted case. These results indicate that modifying CO_2 concentration alone is insufficient to reproduce observed changes. The default parameter set is not tuned to specific observational climatologies, but rather derived from a parameter sweep designed to maximize sensitivity to parameter variations and enable a wide range of experiments within a consistent framework (Hankel et al. 2023).

3.2.1 Comparison with GCM Datasets

Figure 3.7 shows the climatological seasonal cycles of near surface temperature, boundary layer specific humidity, and sea ice fraction for the three analyzed GCMs. Results are presented for both the reference and modern periods of the historical experiment, together with the corresponding CO_2 levels from the 1pctCO2 experiment. The toy model is initialized using parameters derived from each GCM historical simulation. Its seasonal cycles correspond to the final simulation year before reaching the steady state. The toy model reproduces the seasonal cycle of sea ice fraction well across all models and captures near surface temperature variability with slightly lower accuracy. It successfully simulates the late summer and autumn ice free conditions in CMCC, while correctly representing the persistence of sea ice in IPSL and GFDL. inter-model differences in sea ice seasonality are also well reproduced, with larger seasonal amplitudes in IPSL and CMCC compared to GFDL. For near surface temperature, IPSL and GFDL exhibit similar seasonal cycles, which are reasonably well captured by the toy model. The agreement is strongest for CMCC, with r= 0.92 and nRMSE = 0.72. For sea

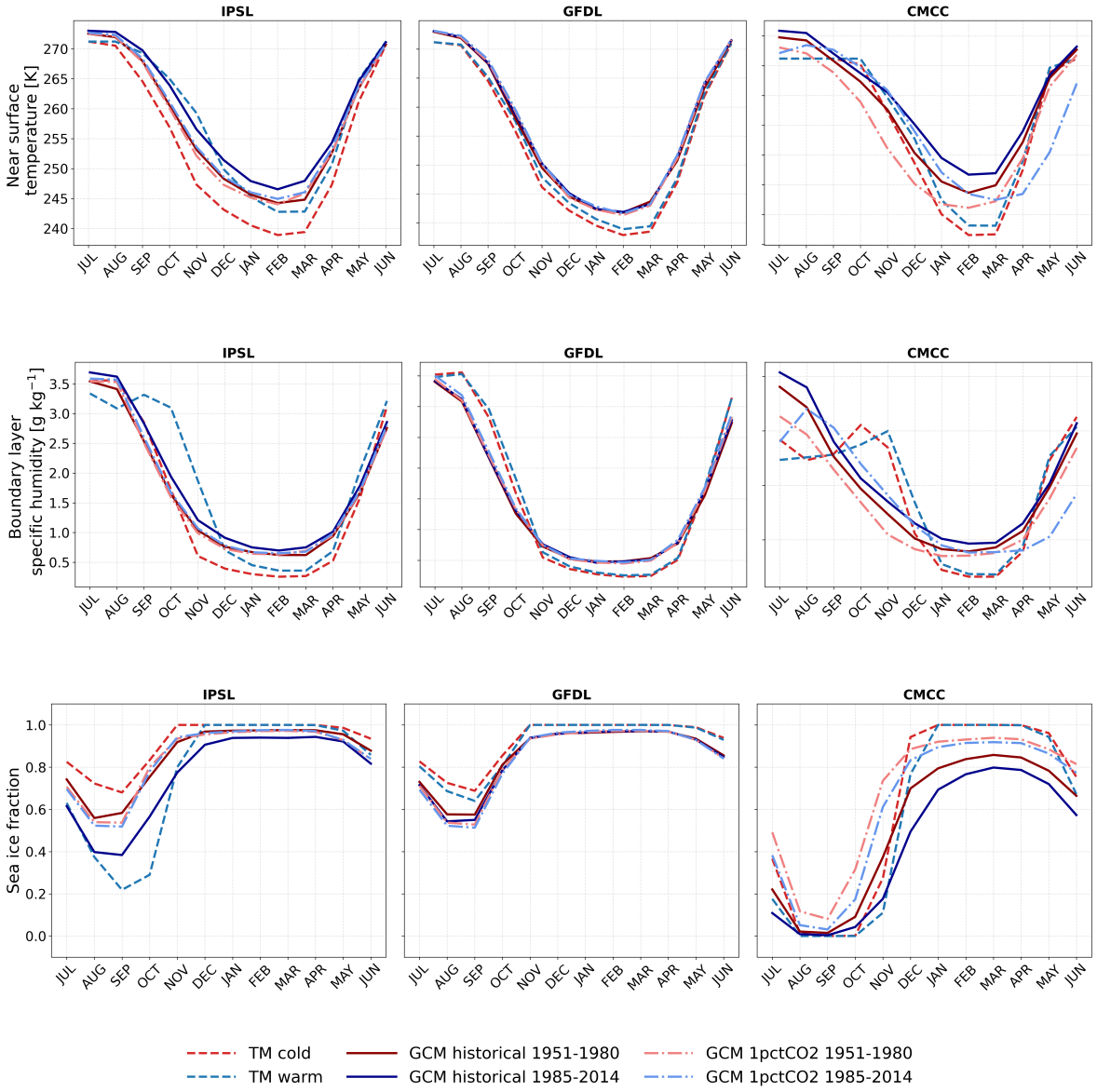

Figure 3.7: Seasonal cycles of near surface air temperature, boundary layer specific humidity, and sea ice fraction from the three GCMs: IPSL-CM6A-LR, GFDL-ESM4, and CMCC-CM2-SR5. Results are shown for both the reference (shades of red) and modern (shades of blue) climatologies of the historical experiment (solid lines), together with the corresponding 30-year windows in terms of CO_2 concentration from the 1pctCO2 experiment (dash–dotted lines). Data are averaged over a band of latitude from 79° N to 81°N. Seasonal cycles from the toy model correspond to the last simulation year before reaching steady state conditions. The toy model is initialized using parameters derived from the GCM historical experiment outputs; toy model seasonal cycles are shown with dashed lines for both the reference (red) and modern (blue) periods.

Variable	Model	r	nRMSE
ΔT_{surf}	IPSL	0.84	3.15
	GFDL	0.41	2.12
	CMCC	0.92	0.72
ΔF_{SI}	IPSL	0.96	2.27
	GFDL	0.96	0.79
	CMCC	0.81	0.91
Δq_{BL}	IPSL	0.44	6.74
	GFDL	0.25	2.75
	CMCC	0.07	3.74

Table 3.5: Correlation coefficient and normalized RMSE between GCM simulations and the GCM adapted toy model steady states for near surface temperature, boundary layer specific humidity, and sea ice fraction change. The metrics are computed from the monthly differences between the warm period (1985-2014) and the cold period (1951-1980). Statistics refer to the data shown in fig. 3.7.

ice fraction, the toy model achieves $r = 0.81$ and nRMSE $= 0.91$ in CMCC, and even higher agreement in GFDL (r$= 0.96$, nRMSE $= 0.79$), indicating a good representation of sea ice response.The toy model struggles in reproducing the seasonal cycle of boundary layer specific humidity. This limitation constrains its ability to represent moisture related processes and may contribute to inconsistencies between simulated variables. The toy model captures generally the timing of summer minima and winter maxima in sea ice, as well as the relative amplitude of seasonal cycles, although magnitudes are generally underestimated, particularly for CMCC. It also reproduces key inter-model differences, with CMCC characterized by warmer conditions and lower sea ice fraction than GFDL. When considering the response to a warmer climate, the toy model generally shows better agreement with the historical experiment than with the 1pctCO2 experiment. Model performance depends on both the variable and the GCM: CMCC shows stronger agreement for temperature but weaker for sea ice, whereas GFDL exhibits the opposite behavior. This suggests that substantial sea ice loss may occur even without strong near surface warming, potentially due to processes not represented in the toy model.

Variable	model	IPSL	GFDL	CMCC	ERA5
T_{surf} (K)	TOY (tuned)	254.3	253.9	260.1	255.6
	GCM-historical	258.0	256.5	262.7	–
	GCM-1pctCO2	257.8	256.7	259.8	–
	Observations	–	–	–	257.5
F_{SI}	TOY (tuned)	0.92	0.92	0.61	0.91
	GCM-historical	0.86	0.85	0.52	–
	GCM-1pctCO2	0.84	0.84	0.67	–
	Observations	–	–	–	0.92

Table 3.6: Annual mean values for near surface temperature, boundary layer specific humidity and sea ice fraction for the 1951-1980 climatology. Results from the toy model tuned to GCMs and ERA5 data, compared with IPSL, GFDL, CMCC 1pctCO2 and historical simulations and ERA5 reanalysis.

variable	model	IPSL	GFDL	CMCC	ERA5
T_{surf} (K)	TOY (tuned)	258.6	254.7	261.3	256.5
	GCM-historical	260.0	256.8	264.7	–
	GCM-1pctCO2	258.5	257.0	261.0	–
	Observations	–	–	–	259.3
F_{SI}	TOY (tuned)	0.76	0.90	0.56	0.81
	GCM-historical	0.76	0.85	0.43	–
	GCM-1pctCO2	0.84	0.84	0.61	–
	Observations	–	–	–	0.83

Table 3.7: Annual mean values for near surface temperature and sea ice fraction for 1985-2014 climatology. Results from the toy model tuned to GCMs and ERA5 data, compared with IPSL, GFDL, CMCC 1pctCO2 and historical simulations and ERA5 reanalysis.

3.2.2 Feedbacks Warming Contributions in the Toy Model

Figure 3.8 shows heat maps of the annual response of near surface temperature and sea ice fraction to individual feedback processes. The response is defined as in eq. 2.29. The toy model is calibrated separately using outputs from each GCM. The y-axis lists the suppressed processes, while the x-axis indicates the GCM used for calibration. Water vapor and lapse rate feedbacks dominate both warming and sea ice loss in the CMCC and IPSL calibrated simulations, consistent with their higher Arctic amplification. GFDL shows much weaker feedback contributions, in line with its lower amplification. IPSL exhibits the strongest impact of heat transport, although it is not the warmest model. This suggests that transport processes play an important role but are not sufficient to explain the overall temperature response within this framework. In GFDL the lapse rate feedback shows a slight positive contribution to near surface temperature but a weak negative contribution to sea ice fraction, indicating an

variable	model	IPSL	GFDL	CMCC	ERA5
ΔT_{surf} (K)	TOY (tuned)	4.31	0.82	1.27	1.10
	GCM-historical	2.00	0.30	2.05	–
	GCM-1pctCO2	0.66	0.33	1.23	–
	Observations	–	–	–	1.78
ΔF_{SI}	TOY (tuned)	-0.15	-0.01	-0.05	-0.10
	GCM-historical	-0.09	-0.01	-0.09	–
	GCM-1pctCO2	0.00	0.00	-0.06	–
	Observations	–	–	–	-0.09

Table 3.8: Annual mean changes for near surface temperature and sea ice fraction between 1951-1980 and 1985-2014 climatologies. Results from the toy model tuned to GCMs and ERA5 data, compared with IPSL, GFDL, CMCC 1pctCO2 and historical simulations and ERA5 reanalysis.

inconsistency between temperature and ice responses. This may reflect delayed or indirectly represented processes. The toy model captures the relative ranking of feedback importance across models, consistent with the seasonal analysis of GCM feedback contributions, although differences in magnitude remain. inter-model differences in both sea ice loss and near surface warming are preserved through the calibrated parameters, indicating that model specific Arctic responses are effectively encoded in the parameters tuning. An important limitation of the toy model is the absence of an explicit representation of global warming, which limits its ability to directly assess Arctic amplification. Nevertheless, it remains a useful framework for investigating Arctic processes through GCM informed parameter calibration.

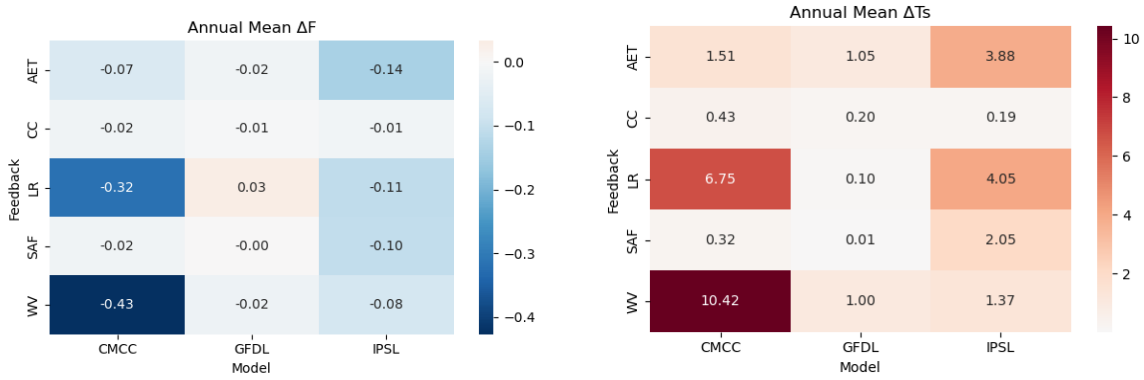

(a) Sea ice fraction annual loss

(b) Near surface temperature annual warming in K

Figure 3.8: Heat maps of annual response to feedback processes in near surface temperature and sea ice fraction. The annual response is $\langle X_{\text{all-fb}} - X_{\text{no-fb}} \rangle$, where X is the state variable.

Chapter 4

Discussion and Conclusions

This study investigated the physical processes controlling Arctic warming and the origin of the inter-model spread in Arctic amplification. The parallel aim is to evaluate whether a conceptual model with reduced complexity can reproduce and help interpret differences across comprehensive climate models and physical processes effect on the climate system. To address this problem, three CMIP6 models characterized by different degrees of Arctic amplification were analyzed: GFDL-ESM4, IPSL-CM6A-LR, and CMCC-CM2-SR5. The models were selected according to the ranking proposed by Linke et al. (2023), which classifies CMIP6 models into CMIP6/w and CMIP6/s groups representing weak and strong Arctic amplification respectively. Arctic amplification was quantified between a reference period (1951–1980) and a modern period (1985–2014), confirming that IPSL and CMCC exhibit stronger amplification than GFDL (Linke et al. 2023). Comparison with ERA5 reanalysis data indicates that models belonging to the strong amplification group reproduce the observed amplification more realistically, whereas GFDL underestimates both Arctic amplification and global warming. Across all models the largest inter-model and intra-model spread occurs during the cold season, which is also the season when Arctic warming reaches its maximum magnitude. When Arctic amplification was evaluated using ratio based and trend based metrics that account for global mean warming, the differences among models were found to arise primarily from differences in Arctic warming itself rather than from differences in global warming. This confirm that the spread in Arctic amplification is controlled by processes acting within the Arctic region, as it is found in Taylor et al. (2022) and Hu et al. (2022). Analyzing the mechanisms responsible for Arctic warming provides further insight into model differences. To evaluate these mechanisms in GCM, the warming contributions of radiative feedbacks and horizontal heat transport anomalies were quantified using the radiative kernel framework imported from Pendergrass et al. (2017). A regional analysis comparing Arctic and tropical responses allowed to distinguish processes specific to polar amplification from those affecting global warming more uniformly. The surface albedo feedback emerges as the dominant contributor to the inter-model spread in Arctic warming on the annual mean. This highlights the representation of sea ice processes and surface albedo changes as an important factor distinguishing climate models. Accurate simu-

lation of sea ice loss therefore appears fundamental for reproducing realistic Arctic warming. The lapse rate feedback also plays a central role in Arctic amplification. It contributes to the contrast between high latitudes and low latitudes warming, because this feedback is positive in the Arctic but negative in the tropics. Although its contribution to inter-model spread is smaller than that of the surface albedo feedback. Most of the differences between models project onto Arctic warming rather than tropical warming, where near-surface temperature responses remain relatively similar across models. Horizontal heat transport anomalies contribute only weakly to the annual mean warming signal; their influence becomes relevant when considering seasonal variability. Seasonal analysis reveals a distinct fingerprint of feedback processes in each model. CMCC, which is the model with the warmest Arctic, shows the largest positive feedback contributions, followed by IPSL, while GFDL exhibits consistently weaker feedbacks, during winter when Arctic warming is strongest. These results further confirm that differences in Arctic warming arise from differences in Arctic feedback processes, and this lead to differences in Arctic amplification more rather than from discrepancies in global temperature change (Taylor et al. 2022; Hu et al. 2022; Linke et al. 2023). Although the surface albedo feedback is not directly active during winter due to the absence of solar radiation, winter still displays the clearest separation among models, particularly through the representation of lapse rate feedback and other positive feedback mechanisms associated with sea ice loss and surface energy exchanges. The lapse rate feedback becomes weakly negative in all models during summer, acting to partially damp warming. The largest inter-model differences in summer arise from the surface albedo feedback, which remains much weaker in GFDL than in IPSL and CMCC. Water vapor feedback maintains the same relative ranking across models but with reduced magnitude compared to winter. Cloud feedbacks exhibit the largest variability among models and represent a major source of uncertainty in Arctic warming projections. In particular longwave cloud feedback is weakly positive in GFDL and IPSL but slightly negative in CMCC, while shortwave cloud feedback ranges from negative in GFDL to strongly positive in CMCC. Even if the annual mean contribution of horizontal heat transport anomalies appears small their seasonal behavior is pronounced. Atmospheric and oceanic heat transport anomalies exhibit opposite signs in winter and summer. In winter atmospheric heat transport anomalies contribute negatively to Arctic warming, while oceanic heat transport anomalies contribute positively. In summer atmospheric heat transport becomes the largest warming contribution, whereas oceanic heat transport is strongly negative. The weak annual mean signal therefore results from seasonal compensation between opposite contributions. This seasonal redistribution of heat may also contribute to delayed winter warming, as heat absorbed by the ocean during summer can be released during the cold season, enhancing surface warming and sea ice loss. Given the substantial inter-model differences in Arctic warming, the simplified framework developed by Hankel et al. (2023) was employed to investigate the processes involved in Arctic climate response. A vertically resolved single column conceptual model was used, representing the coupled evolution of the ocean mixed layer, sea ice, and atmosphere at 80°N. Model parameters were calibrated using ERA5 reanalysis and GCMs outputs for both reference and modern periods. In its default configuration the conceptual model does not re-

produce observed seasonal cycles accurately. After calibration using observationally derived parameters the model captures the qualitative response of near surface temperature and sea ice concentration to a warmer climate. When initialized with parameters derived from individual GCMs, the conceptual model reproduces the relative differences among the three models. In particular simulations calibrated with IPSL and CMCC parameters produce warmer Arctic conditions and reduced sea ice fractions compared with GFDL based simulations. The conceptual model underestimates absolute temperatures and struggles to reproduce boundary layer humidity. Overall it successfully captures the relative ranking of Arctic warming and sea ice loss across models. The calibrated parameters therefore implicitly encode the different responses of the GCMs to a warming climate. Within this simplified framework a set of mechanism denial experiments was performed to isolate the impact of individual feedback processes. These experiments suppress specific processes such as cloud feedback, lapse rate feedback, surface albedo feedback, water vapor feedback, and atmospheric heat transport, and evaluate the resulting equilibrium response of the model. Unlike radiative kernel diagnostics, which attribute warming within the radiative budget, this approach evaluates the influence of feedback processes on the steady state climate response of the system, allowing delayed responses and interactions among processes to emerge. The mechanism denial experiments indicate that lapse rate and water vapor feedbacks produce the strongest impact on Arctic warming in the conceptual model, while the surface albedo feedback plays a more limited role. In particular the albedo feedback produces a strong response primarily in simulations calibrated with IPSL parameters. IPSL is the model with the strongest Arctic amplification among the selected CMIP6 models, although it does not exhibit the warmest Arctic conditions. This result suggests that surface albedo feedback is particularly important for enhancing Arctic amplification rather than being the sole driver of absolute Arctic warming. While lapse rate and water vapor feedbacks contribute substantially to Arctic temperature increases, surface albedo feedback strengthens the contrast between Arctic and global warming. The conceptual model successfully captures the relative ranking of feedback structure. The conceptual model also reproduces the qualitative influence of atmospheric heat transport differences among models. IPSL simulations show stronger transport anomalies than the other models, yet IPSL is not the warmest model overall. This indicates that atmospheric transport can significantly affect Arctic temperature but does not solely determine the final warming response. Overall the conceptual model reproduces the qualitative behavior and relative Arctic warming strength of the three analyzed GCMs when driven by parameters derived from them, while quantitative agreement remains limited, particularly for CMCC. The results demonstrate that the dominant feedback structure and seasonal response of comprehensive climate models can be meaningfully captured within a reduced complexity framework. Some limitations make it necessary to use this simplified framework in combination with complementary tools for climate analysis. The conceptual model represents only a single Arctic column and does not explicitly simulate the evolution of global mean temperature. Indeed Arctic amplification relative to global warming cannot be directly analyzed within the model. In addition the simplified atmospheric representation limits the accuracy of humidity and cloud processes. Future developments could extend the

model by including additional spatial domains or simplified representations of lower latitudes and land processes. Such extensions would allow Arctic and global warming to be analyzed simultaneously within a unified and computationally efficient framework.

Finally the results of this study confirm that differences in Arctic feedback processes are a main driver of the inter-model spread in Arctic amplification. This spread arises primarily from differences in the representation of Arctic warming rather than from differences in global warming. Surface albedo feedback emerges as the main driver of inter-model variability, while lapse rate and water vapor feedbacks play a key role in determining the magnitude of Arctic warming. Seasonal heat storage and release in the ocean further contribute to the characteristic winter maximum of Arctic amplification. By linking GCM diagnostics with a reduced complexity conceptual model, this work demonstrates that simplified frameworks can provide valuable insight into the physical mechanisms controlling Arctic climate change and the sources of uncertainty in climate model projections.

Chapter 5

Appendix

Construction of the datasets for pre-computed radiative kernel

The radiative kernel code requires two input datasets in netCDF format called basefields.nc and changefields.nc. These files describe the mean climate state of a reference period and the corresponding changes in a later period. Both files must contain the same variables, dimensions and metadata structure. The variables include surface fluxes, atmospheric temperature, water vapor mixing ratio and coordinate fields. The vertical coordinate is defined by the model pressure levels that are provided as an array.

The file basefields.nc represents the mean climate state during the reference period. In this work the reference period is the interval 1951 to 1980 from the historical simulations of CMCC, IPSL and GFDL. For each model monthly means are computed for all fields and then averaged across the full 30 year period. The resulting multi year mean fields are written into basefields.nc using the same variable names and dimensions as in the original CESM kernel dataset. The time dimension contains twelve representative monthly means and all fields follow the standard units and metadata conventions used in CMIP style model output. The file changefields.nc contains the anomalies relative to the reference period. The change period used is the interval 1985 to 2014 from the historical simulations. For each model monthly means are computed for the change period and then subtracted from the corresponding monthly means of the reference period. The resulting differences in temperature, water vapor, surface temperature and radiative fluxes are written into changefields.nc. The structure of this file is identical to basefields.nc so that the kernel code can read both files without modification.

Interpolation onto the CESM kernel grid

In order to use the CESM radiative kernels, all GFDL-ESM4, CMCC-CM2-SR5 and IPSL-CM6A-LR fields must be expressed on the same horizontal grid and on the same fixed pressure levels as the kernels. This is achieved in two steps: first, horizontal regridding to the kernel latitude and longitude grid, and then vertical interpolation from the native GCM pressure levels to the fixed kernel pressure levels.

Regarding the horizontal interpolation: let $X^{\mathrm{src}}(t,\phi_s,\lambda_s)$ be a generic 2D or 3D field on the GFDL, IPSL or CMCC grid, where ϕ_s and λ_s denote the latitude and longitude, and t is the (monthly) time index. The CESM kernels are defined on a target grid (ϕ_k,λ_k) read from t.kernel.nc available at Pendergrass et al. (2017). The horizontal regridding is performed with a bilinear interpolation scheme as implemented in xESMF python library (COECMS 2024). For each target grid point (ϕ_k,λ_k), the interpolated value is a weighted sum of the four nearest source grid points:

$$X^{\mathrm{2D}}(t,\phi_k,\lambda_k) \;=\; \sum_{m=1}^{4} w_m(\phi_k,\lambda_k)\,X^{\mathrm{src}}(t,\phi_{s,m},\lambda_{s,m}), \tag{5.1}$$

where the weights w_m depend only on the relative position of the target point within the surrounding source grid cell and satisfy

$$\sum_{m=1}^{4} w_m(\phi_k,\lambda_k) = 1. \tag{5.2}$$

This step is applied separately to each variable and to each monthly climatology. Regarding the vertical interpolation i followed the steps used in the ncl script given by Pendergrass et al. (2017), the CESM kernels are provided on a set of fixed pressure levels p_i^{ker} (Pendergrass 2017b). The atmospheric temperature T and specific humidity Q for the GCMs are originally defined on model N_{src} pressure levels p_j^{src}, stored as plev in Pa. I first convert them to hPa because the kernels levels are in hPa. For each time, latitude, and longitude point (t,ϕ_k,λ_k) I consider the vertical profile

$$X_j = X(t,p_j,\phi_k,\lambda_k) \tag{5.3}$$

where X stands for T or Q. I then interpolate this profile from the native levels p_j^{src} to the kernel levels p_i^{ker} using a linear interpolation in logarithmic pressure ($\tilde{p}_j = \ln p_j$). The interpolated value at a target level p_i^{ker} is given by $X\left(\tilde{p}_i^{\mathrm{ker}}\right)$, where $X(\tilde{p})$ is defined by the linear interpolation between the known points $(\tilde{p}_j, X_j)$:

$$X(\tilde{p}) = X_j + \frac{\tilde{p}-\tilde{p}_j}{\tilde{p}_{j+1}-\tilde{p}_j}\left(X_{j+1}-X_j\right) \quad \text{for} \quad \tilde{p}_j \le \tilde{p} \le \tilde{p}_{j+1}. \tag{5.4}$$

For pressures outside the native range, a linear extrapolation in $\ln p$ is used.

Finally, all fields are masked south of 66°N by setting them to NaN, so that the resulting dataset only covers the Arctic domain.

Toy model Parameters

Table 5.1: List of model parameters used in the sensitivity analysis. Each parameter includes its name, symbol, and description with default value.

Category	Symbol	Description (default value)
Ice	H_{min}	Minimum ice thickness (0.75 m)
	α_{mp}	Albedo of melt ponds (0.5)
	α_{ice}	Albedo of bare ice (0.725)
Ocean	D	Slab ocean depth (100 m)
	α_o	Surface albedo of the ocean (0.15)
	τ_f	Timescale of ocean-ice heat exchange (4 weeks)
	τ_o	Timescale of ocean poleward heat flux (1.3 years)
	$\text{T}_{\text{mid,o}}$	Midlatitude ocean reference temperature (275 K)
	y	Latitude used in seasonal cycle (80°N)
Atmosphere	v_H	Wind velocity scale (7.5 m/s)
	τ_a	Timescale of atmospheric poleward heat flux (4 weeks)
	τ_p	Precipitation timescale (3 hours)
	$\text{T}_{\text{mid,bl}}$	Midlatitude boundary layer temperature (280 K)
	ΔT_{dbl}	Warming per CO_2 doubling (2.5 K)
	R	Relative humidity threshold for precipitation (0.8)
	ε_0	Clear-sky emissivity without CO_2 and H_2O
	RH_{atm}	Relative humidity in the troposphere (0.4)
	RH_{bl}	Relative humidity in boundary layer (0.8)
	q_0	Specific humidity threshold for GHG effect (0.0002 kg/kg)
	α_{cld}	Albedo of low clouds (0.15)
	$\Delta\varepsilon_0$	Max emissivity change due to clouds (0.2)
	$\varepsilon_{\text{H}_2\text{O}}$	Water vapor emissivity (0.072) [Eq. 2.4]
	$\varepsilon_{\text{CO}_2}$	CO_2 emissivity (0.041) [Eq. 2.4]
	ΔQ	Max convective flux affecting cloud emissivity (0.0002 kg/kg)

Radiative diagnostics in GCMs

Surface albedo is defined for all-sky (α_{sfc}) is computed as

$$\alpha_{\text{sfc}} = \frac{\text{RSUS}}{\text{RSDS}}, \tag{5.5}$$

where RSUS is the upwelling shortwave flux at the surface and RSDS is the downwelling shortwave flux at the surface. The clear-sky surface albedo is calculated analogously as

$$\alpha_{\text{sfc}}^{\text{cs}} = \frac{\text{RSUSCS}}{\text{RSDSCS}}, \tag{5.6}$$

using clear-sky fluxes only. Grid points where the incoming shortwave flux is zero are excluded to avoid division by zero.

At the TOA the planetary albedo in all-sky condition (α_{TOA}) is defined as

$$\alpha_{\mathrm{TOA}} = \frac{\mathrm{RSUT}}{\mathrm{RSDT}}, \tag{5.7}$$

where RSUT is the upwelling shortwave flux at TOA and RSDT is the incoming solar flux at TOA. The clear-sky TOA albedo is equivalently defined as

$$\alpha^{\mathrm{cs}}_{\mathrm{TOA}} = \frac{\mathrm{RSUTCS}}{\mathrm{RSDT}}. \tag{5.8}$$

(Pharr et al. 2004). An effective atmospheric emissivity is diagnosed from the downwelling longwave radiation at the surface. Assuming blackbody emission at the surface temperature of the model, the all-sky effective emissivity ε is computed as

$$\varepsilon = \frac{\mathrm{RLDS}}{\sigma T_s^4}, \tag{5.9}$$

where RLDS is the downwelling longwave radiation at the surface, σ is the Stefan Boltzmann constant, and T_s is the near surface air temperature. The clear-sky effective emissivity is defined analogously as

$$\varepsilon^{\mathrm{cs}} = \frac{\mathrm{RLDSCS}}{\sigma T_s^4}. \tag{5.10}$$

(Wallace et al. 2006) Diagnostics are computed for both reference (1951-1980) and modern (1985-2014) climatologies using the historical experiment. To substitute the GCM radiative diagnostics as parameters in the toy model, an average from 79 ° to 81° N is performed to have the mean albedos and emissivity at 80° N.

Parameter	**GFDL**		**IPSL**		**CMCC**		**ERA5**	
	(1951-1980)	(1985-2014)	(1951-1980)	(1985-2014)	(1951-1980)	(1985-2014)	(1951-1980)	(1985-2014)
$\alpha_{ice,0}$	0.64	0.63	0.66	0.62	0.46	0.43	0.66	0.61
ε_0	0.71	0.71	0.71	0.72	0.70	0.72	0.02	0.02
CO_2 (ppm)	320	362	320	368	320	365	319	360
α_{cld}	0.09	0.09	0.07	0.08	0.10	0.10	0.08	0.09
$\Delta\varepsilon_{cld}$	0.16	0.16	0.13	0.14	0.11	0.12	0.01	0.01
d (m)	18	18	14	14	13	13	12	12
ΔT_{mid} (K)	18	18	14	14	13	13	12	12

Table 5.2: Initializing parameters for the toy model from GCMs' output

Acknowledgments

I would like to sincerely thank my thesis supervisors Paolo Ruggieri and Guillaume Gastineau for their kindness, care, and the attention with which they inspired and guided me throughout this work. I would also like to express my special thanks to Nicolas Michalezyk and Martin Vancoppenolle for their support during my internship. I am grateful for the opportunity to have carried out my internship at the LOCEAN laboratory, and I would like to thank the colleagues there who warmly welcomed me during this time and contributed to creating a stimulating and supportive environment.

Finally I would like to thank my family and all my friends, there will be the time and space to properly thank you for everything.

Bibliography

Ackerman, S. and J. A. Knox (2006). *Meteorology: Understanding the Atmosphere*. Cengage Learning.

Adcroft, A. et al. (2019). "Model description and simulation features". In: *Journal of Advances in Modeling Earth Systems* 11, pp. 3167–3211. DOI: 10.1029/2019MS001726.

Andrews, T., J. M. Gregory, and M. J. Webb (2015). "The Dependence of Radiative Forcing and Feedback on Evolving Patterns of Surface Temperature Change in Climate Models". In: *Journal of Climate* 28.4. DOI: 10.1175/JCLI-D-14-00545.1.

Bates, J. R. (2007). "Some considerations of the concept of climate feedback". In: *Quarterly Journal of the Royal Meteorological Society* 133.624. DOI: 10.1002/qj.62.

Beer, E. and I. Eisenman (2022). "Revisiting the Role of the Water Vapor and Lapse Rate Feedbacks in the Arctic Amplification of Climate Change". In: *Journal of Climate* 35.9, pp. 2975–2988. DOI: 10.1175/JCLI-D-21-0814.1.

Bintanja, R., R. G. Graversen, and W. Hazeleger (2011). "Arctic winter warming amplified by the thermal inversion and consequent low infrared cooling to space". In: *Nature Geoscience* 4.11, pp. 758–761. DOI: 10.1038/ngeo1285.

Bitz, C. M. and G. H. Roe (2004). "A mechanism for the high rate of sea ice thinning in the Arctic Ocean". In: *Journal of Climate* 17, pp. 3623–2632. DOI: 10.1175/1520-0442(2004)017<3623:AMFTHR>2.0.CO;2.

Block, K. et al. (2020). "Climate models disagree on the sign of total radiative feedback in the Arctic". In: *Tellus A: Dynamic Meteorology and Oceanography* 72.1, pp. 1–14. DOI: 10.1080/16000870.2019.1696139.

Boeke, R. C. and P. C. Taylor (2018). "Seasonal energy exchange in sea ice retreat regions contributes to differences in projected Arctic warming". In: *Nature communications* 9, 5017. DOI: 10.1038/s41467-018-07061-9.

Boeke, R. C., P. C. Taylor, and S. A. Sejas (2021). "On the Nature of the Arctic's Positive Lapse-Rate Feedback". In: *Geophysical Research Letters*. DOI: 10.1029/2020GL091109.

Boeke, R. and P. C. Taylor (2016). "Evaluation of the Arctic surface radiation budget in CMIP5 models". In: *Geophysical Research Letters* 121.14. DOI: 10.1002/2016JD025099.

Boitsov, V. D., A. L. Karsakov, and G. Trofimov (2012). "Atlantic water temperature and climate in the Barents Sea, 2000–2009". In: *ICES Journal of Marine Science* 69.5, pp. 833–840. DOI: 10.1093/icesjms/fss075.

Bonan, D. B. et al. (2018). "Sources of Uncertainty in the Meridional Pattern of Climate Change". In: *Geophysical Research Letters* 45.17. DOI: 10.1029/2018GL079429.

Bonan, D. et al. (2025). "Mid-latitude clouds contribute to Arctic amplification via interactions with other climate feedbacks". In: *Environmental Research Climate* 4. DOI: 10.1088/2752-5295/ada84b.

Boucher, O. et al. (2020). "Presentation and Evaluation of the IPSL-CM6A-LR Climate Model". In: *Journal of Advances in Modeling Earth System* 12. DOI: 10.1029/2019MS002010.

Budyko, M. I. (1961). "The Heat Balance of the Earth's Surface". In: *Soviet Geography* 2.4. DOI: 10.1080/00385417.1961.10770761.

Carvalho, K. S. and S. Wang (2020). "Sea surface temperature variability in the Arctic Ocean and its marginal seas in a changing climate: Patterns and mechanisms". In: *Global and Planetary Change* 193. DOI: 10.1016/j.gloplacha.2020.103265.

Cheng, K. et al. (2025). "Distinct Impacts of Increased Atlantic and Pacific Ocean Heat Transport on Arctic Ocean Warming and Sea Ice Decline". In: *JGR Oceans* 130.23. DOI: 10.1029/2024JC021178.

Cherchi, A. et al. (2019). "Global Mean Climate and Main Patterns of Variability in the CMCC-CM2 Coupled Model". In: *Journal of Advances in Modeling Earth Systems* 11, pp. 185–209. DOI: 10.1029/2018MS001369.

Chung, E. et al. (2025). "The role of sea ice in present and future Arctic amplification". In: *Communications Earth and Environment* 6,910. DOI: 10.1038/s43247-025-02834-9.

Chylek, P. et al. (2009). "Arctic air temperature change amplification and the Atlantic Multidecadal Oscillation". In: *Geophysical Research Letters* 36. DOI: 10.1029/2009GL038777.

Chylek, P. et al. (2024). "High Values of the Arctic Amplification in the Early Decades of the 21st Century: Causes of Discrepancy by CMIP6 Models Between Observation and Simulation". In: *Advanced Earth and Space Sciences*. DOI: 10.1029/2023JD039269.

Claussen, M. et al. (2002). "Earth system models of intermediate complexity: closing the gap in the spectrum of climate system models". In: *Climate Dynamics* 5, pp. 579–586. DOI: 10.1007/s00382-001-0200-1.

CMCC (2016). *CMIP6 ScenarioMIP output from CMCC-CM2-SR5 model*. DOI: 10.22033/ESGF/CMIP6.1365.

COECMS (2024). *Regridding with xESMF*. URL: https://coecms-training.github.io/parallel/case-studies/regridding.html.

Cohen, J. et al. (2020). "Divergent consensuses on Arctic amplification influence on midlatitude severe winter weather". In: *Nature Climate Change* 10, pp. 20–29. DOI: 10.1038/s41558-019-0662-y.

Colman, R. A. and B. J. McAvaney (2011). "On tropospheric adjustment to forcing and climate feedbacks". In: *Climate Dynamics* 36, pp. 1649–1658. DOI: 10.1007/s00382-011-1067-4.

Community Earth System Model developers and affiliates (2019). *CMIP6 CESM2 1pctCO2 experiment with high-top atmosphere (WACCM6) with interactive chemistry (TSMLT1), interactive land (CLM5), coupled ocean (POP2) with biogeochemistry (MARBL), inter-*

active sea ice (CICE5.1), and non-evolving land ice (CISM2.1). URL: https://data.ucar.edu/en/dataset/cmip6-cesm2-1pctco2-experiment-with-high-top-atmosphere-waccm6-with-interactive-chemistry-tsmlt.

Coulbury, C. and I. Tan (2024). "Top of the Atmosphere Shortwave Arctic Cloud Feedbacks: A Comparison of Diagnostic Methods". In: *Geophysical Research Letters* 51.10. DOI: 10.1029/2023GL107780.

Craig, A. P., M. Vertenstein, and R. Jacob (2012). "A new flexible coupler for Earth system modeling developed for CCSM4 and CESM1." In: *International Journal of High Performance Computing* 26.1, pp. 31–42. DOI: 10.1177/1094342011428141.

Crook, J. A. and P. M. Forster (2011). "A Balance between Radiative Forcing and Climate Feedback in the Modeled 20th Century Temperature Response". In: *Journal of Geophysical Research: Atmospheres* 116, p. D17108. DOI: 10.1029/2011JD015924. URL: https://doi.org/10.1029/2011JD015924.

Curry, J. et al. (1995). "Water vapor feedback over the Arctic Ocean". In: *Journal of Geophysical Research Atmospheres* 100.7. DOI: 10.1029/95JD00824.

Davy, R. and I. Esau (2018). "Differences in the efficacy of climate forcings explained by variations in atmospheric boundary layer depth". In: *Nature Communications* 9, p. 685. DOI: 10.1038/s41467-017-02692-z.

Donner, L. J., W. H. Schubert, and R. Somerville (2011). *The Development of Atmospheric General Circulation Models: Complexity, Synthesis and Computation*. Cambridge University Press.

Druckenmiller, M. L., R. L. Thoman, and T. A. Moon (2025). "2025: Arctic Report Card". In: *Coordinating Eds.* DOI: 10.25923/nrzf-j897.

Dunne, J. P. et al. (2020). "The GFDL Earth System Model Version 4.1 (GFDL-ESM4.1): Overall Coupled Model Description and Simulation Characteristics". In: *Journal of Advances in Modeling Earth System* 12. DOI: 10.1029/2019MS002015.

Eastman, R. and S. G. Warren (2010). "Interannual Variations of Arctic Cloud Types in Relation to Sea Ice". In: *Journal of Climate* 23.16, pp. 4216–4232. DOI: 10.1175/2010JCLI3492.1.

Eby, M. et al. (2013). "Historical and idealized climate model experiments: an intercomparison of Earth system models of intermediate complexity". In: *Climate of the past* 9, pp. 1111–1140. DOI: 10.5194/cp-9-1111-2013.

Eisenman, I. and J. S. Wettlaufer (2009). "Nonlinear threshold behavior during the loss of Arctic sea ice". In: *Proceedings of the National Academy of Sciences of the United States of America* 106.1, pp. 28–32. DOI: 10.1073/pnas.0806887106.

Feldl, N., S. Bordoni, and T. M. Merlis (2017). "Coupled high-latitude climate feedbacks and their impact on atmospheric heat transport". In: *Journal of Climate* 30.1, pp. 189–201. DOI: 10.1175/JCLI-D-16-0324.1.

Feldl, N. and T. Merlis (2021). "Polar Amplification in Idealized Climates: The Role of Ice, Moisture, and Seasons". In: *Geophysical Research Letters* 48. DOI: 10.1029/2021GL094130.

Feldl, N. and G. H. Roe (2013). “Four Perspectives on Climate Feedbacks”. In: *Geophysical Research Letters* 40, pp. 4007–4011. DOI: 10.1002/grl.50711.

Feldl, N. et al. (2020). “Sea ice and atmospheric circulation shape the high-latitude lapse rate feedback”. In: *NPJ Climate and Atmospheric Science*, pp. 1–9. DOI: 10.1038/s41612-020-00146-7.

Fernandez-Granja, J. et al. (2021). “Improved atmospheric circulation over Europe by the new generation of CMIP6 earth system models”. In: *Climate Dynamics* 56, pp. 3527–3540. DOI: 10.1007/s00382-021-05652-9.

Flato, G. M. (2011). “Earth system models: an overview”. In: *WIREs Climate Change* 2.6. DOI: 10.1002/wcc.148.

Francis, J. A. and S. J. Vavrus (2015). “Evidence for a Wavier Jet Stream in Response to Rapid Arctic Warming”. In: *Environmental Research Letters* 10.1, p. 014005. DOI: 10.1088/1748-9326/10/1/014005.

Goodwin, P. and R. G. Williams (2023). “On the Arctic Amplification of surface warming in a conceptual climate model”. In: *Physica D: Nonlinear Phenomena* 454. DOI: 10.1016/j.physd.2023.133880.

Goosse, H. and V. Zunz (2014). “Decadal trends in the Antarctic sea ice extent ultimately controlled by ice–ocean feedback”. In: *Cryosphere* 8, pp. 453–470. DOI: 10.5194/tc-8-453-2014.

Goosse, H. et al. (2018). “Quantifying climate feedbacks in polar regions”. In: *Nature Communications* 9.1919. DOI: 10.1038/s41467-018-04173-0.

Graff, L. S. et al. (2025). “Sensitivity of winter Arctic amplification in NorESM2”. In: *EGUsphere*. DOI: 10.5194/egusphere-2025-472.

Graversen, R. G., P. L. Langen, and T. Mauritsen (2014). “Polar Amplification in CCSM4: Contributions from the Lapse Rate and Surface Albedo Feedbacks”. In: *Journal of Climate* 27.12, pp. 4433–4450. DOI: 10.1175/JCLI-D-13-00551.1.

Graversen, R. G. and M. Wang (2009). “Polar amplification in a coupled climate model with locked albedo”. In: *Climate Dynamics* 33, pp. 629–643. DOI: 10.1007/s00382-009-0535-6.

Gregory, J. M., T. Andrews, and P. Good (2015). “The inconstancy of the transient climate response parameter under increasing CO2”. In: *Philosophical Transactions of the Royal Society* 373.2054. DOI: 10.1098/rsta.2014.0417.

Gregory, J. M. et al. (2004). “A New Method for Diagnosing Radiative Forcing and Climate Sensitivity”. In: *Geophysical Research Letters* 31, p. L03205. DOI: 10.1029/2003GL018747.

Hahn, L. C. et al. (2021). “Contributions to Polar Amplification in CMIP5 and CMIP6 Models”. In: *Frontiers in Earth Science* 9, p. 710036. DOI: 10.3389/feart.2021.710036.

Haine, T. W. N. (2021). “A Conceptual Model of Polar Overturning Circulations”. In: *Journal of Physical Oceanography* 51.3. DOI: 10.1175/JPO-D-20-0139.1.

Hall, A. (2004). “The Role of Surface Albedo Feedback in Climate”. In: *Journal of Climate* 17.7, pp. 1550–1568. DOI: 10.1175/1520-0442(2004)017<1550:TROSAF>2.0.CO;2.

Hankel, C. and E. Tziperman (2023). “Assessing the Robustness of Arctic Sea Ice Bi-Stability in the Presence of Atmospheric Feedbacks”. In: *Journal of Geophysical Research: Atmospheres* 128.21. DOI: 10.1029/2023JD039337.

Hansen, J. et al. (1984). “Climate Sensitivity: Analysis of Feedback Mechanisms”. In: *Climate Processes and Climate Sensitivity* 29. DOI: 10.1029/GM029p0130.

He, S. et al. (2020). “Eurasia cooling linked to the vertical distribution of Arctic warming.” In: *Geophysical Research Letters* 47. DOI: 10.1029/2020gl087212.

Heinze, C. et al. (2019). “ESD Reviews: Climate feedbacks in the Earth system and prospects for their evaluation”. In: *Earth System Dynamics* 10, pp. 379–452. DOI: 10.5194/esd-10-379-2019.

Henderson, G. R. et al. (2021). “Local and Remote Atmospheric Circulation Drivers of Arctic Change: A Review”. In: *Frontiers in Earth Science* 9. DOI: 10.3389/feart.2021.709896.

Henry, M. and T. M. Merlis (2020). “Forcing Dependence of Atmospheric Lapse Rate Changes Dominates Residual Polar Warming in Solar Radiation Management Climate Scenarios”. In: *Geophysical Research Letters* 47.15. DOI: 10.1029/2020GL087929.

Hersbach, H. et al. (2020). “The ERA5 global reanalysis”. In: *Quarterly Journal of the Royal Meteorological Society* 146.730. DOI: 10.1002/qj.3803.

Hind, A. et al. (2016). “Arctic amplification and its possible causes: An assessment of CMIP5 model performance”. In: *Geophysical Research Letters* 43.13, pp. 7163–7170. DOI: 10.1002/2016GL069241.

Holland, M. M. and C. M. Bitz (2003). “Polar amplification of climate change in coupled model”. In: *Climate Dynamics* 21, pp. 221–232. DOI: 10.1007/s00382-003-0332-6.

Hu, X. et al. (2022). “A Quantitative Analysis of the Source of Inter-Model Spread in Arctic Surface Warming Response to Increased CO2 Concentration”. In: *Geophysical Research Letters*. DOI: 10.1029/2022GL100034.

Huang, Y. et al. (2017). “Estimation of radiative feedbacks using radiative kernels based on ERA-Interim reanalysis”. In: *Journal of Climate* 30.14, pp. 5435–5452. DOI: 10.1175/JCLI-D-16-0208.1.

Hunke, E. and W. Lipscomb (2008). *CICE: The Los Alamos sea ice model, documentation and software, version 4.0.* Tech. rep. Los Alamos National Laboratory, Technical Report LA-CC-06-012.

Huo, Y. et al. (2024). “Assessing Radiative Feedbacks and Their Contribution to the Arctic Amplification Measured by Various Metrics”. In: *Journal of Geophysical Research: Atmospheres* 129, e2024JD040880. DOI: 10.1029/2024JD040880.

Hwang, Y. and D. M. W. Frierson (2010). “Increasing atmospheric poleward energy transport with global warming.” In: *Geophysical Research Letters* 37.24. DOI: 10.1029/2010GL045440.

Hwang, Y., D. M. W. Frierson, and J. E. Kay (2011). “Coupling between Arctic feedbacks and changes in poleward energy transport”. In: *Geophysical Research Letters* 38.17. DOI: 10.1029/2011GL048546.

IPCC (2019). *Special Report on the Ocean and Cryosphere in a Changing Climate*. URL: https://www.ipcc.ch/srocc/.

Iqbal, Z. et al. (2020). "Evaluation of global climate models for precipitation projection in sub-Himalaya region of Pakistan". In: *Atmospheric Research* 245.105061. DOI: 10.1016/j.atmosres.2020.105061.

Ivanov, V. et al. (2015). "Arctic Ocean Heat Impact on Regional Ice Decay: A Suggested Positive Feedback". In: *Journal of Physical Oceanography* 46.5. DOI: 10.1175/JPO-D-15-0144.1.

Jenkins, M. and A. Dai (2021). "The Impact of Sea-Ice Loss on Arctic Climate Feedbacks and Their Role for Arctic Amplification". In: *Geophysical Research Letters* 48.15. DOI: 10.1029/2021GL094599.

Johannessen, O. M. et al. (2016). "Surface air temperature variability and trends in the Arctic: New amplification assessment and regionalization". In: *Tellus A: Dynamic Meteorology and Oceanography* 68.1, p. 28234. DOI: 10.3402/tellusa.v68.28234.

Kay, J. E. et al. (2016). "Recent Advances in Arctic Cloud and Climate Research". In: *Current Climate Change Report* 2, pp. 159–169. DOI: 10.1007/s40641-016-0051-9.

Khan, N. et al. (2025). "Global climate models performance: A comprehensive review of applied approaches, recognized issues and possible future directions". In: *Atmospheric Research* 326. DOI: 10.1016/j.atmosres.2025.108300.

Kivimaa, P. et al. (2024). "Evaluating policy coherence and integration for adaptation: the case of EU policies and Arctic cross-border climate change impacts". In: *Climate Policy* 25, pp. 59–75. DOI: 10.1080/14693062.2024.2337168.

Labe, Z., Y. Peings, and G. Magnusdottir (2020). "Warm Arctic, Cold Siberia Pattern: Role of Full Arctic Amplification Versus Sea Ice Loss Alone". In: *Geophysical Research Letters* 47.17. DOI: 10.1029/2020GL088583.

Laîné, A., M. Yoshimori, and A. Abe-Ouchi (2016). "Surface Arctic amplification factors in CMIP5 models: land and oceanic surfaces and seasonality". In: *Journal of Climate* 29, pp. 3297–3316. DOI: 10.1175/JCLI-D-15-0497.1.

Lauer, M. et al. (2020). "CO2-forced changes of Arctic temperature lapse-rates in CMIP5 models". In: *Meteorologische Zeitschrift*, pp. 79–93. DOI: 10.1127/metz/2020/0975.

Lecomte, O. et al. (2017). "Vertical ocean heat redistribution sustaining sea-ice concentration trends in the Ross Sea". In: *Nature* 8.258. DOI: 10.1038/s41467-017-00347-4.

Linke, O. et al. (2023). "Constraints on simulated past Arctic amplification and lapse rate feedback from observations". In: *Atmospheric Chemistry and Physics* 23, pp. 9963–9992. DOI: 10.5194/acp-23-9963-2023.

Liu, Y., J. R. Key, and X. Wang (2008). "The Influence of Changes in Cloud Cover on Recent Surface Temperature Trends in the Arctic". In: *Journal of Climate* 21, pp. 705–724. DOI: 10.1175/2007JCLI1681.1.

Lu, J. and M. Cai (2009). "A New Framework for Isolating Individual Feedback Processes in Coupled General Circulation Climate Models. Part I: Formulation". In: *Climate Dynamics* 32, pp. 873–885. DOI: 10.1007/s00382-008-0425-3.

Madec, G. and M. Imbard (1996). "A global ocean mesh to overcome the North Pole singularity". In: *Climate Dynamics* 12, pp. 381–388. DOI: 10.1007/BF00211684.

Madec, G. and N. Team (2016). *NEMO Ocean Engine*. Tech. rep. Institut Pierre-Simon Laplace (IPSL).

Martinson, D. G. (1990). "Evolution of the Southern Ocean winter mixed layer and sea ice-open ocean deep-water formation and ventilation". In: *Journal of Geophysical Research Oceans* 95, pp. 11641–11654. DOI: 10.1029/JC095iC07p11641.

Matishov, G. G. et al. (2014). "Pronounced anomalies of air, water, ice conditions in the Barents and Kara Seas, and the Sea of Azov". In: *Oceanologia* 56.3. DOI: doi.org/10.5697/oc.56-3.445.

Matthews, J. B. R. et al. (2021). "Annex VII: Glossary". In: *Climate Change 2021: The Physical Science Basis*. Cambridge University Press, pp. 2215–2256. DOI: 10.1017/9781009157896.022.

McKenney, D. W. et al. (2011). "Revisiting projected shifts in the climate envelopes of North American trees using updated general circulation models". In: *Global Change Biology* 17.8. DOI: 10.1111/j.1365-2486.2011.02413.x.

Meraner, K., T. Mauritsen, and A. Voigt (2013). "Robust increase in equilibrium climate sensitivity under global warming". In: *Geophysical Research Letters* 40.22. DOI: 10.1002/2013GL058118.

Mewes, D. and C. Jacobi (2019). "Heat transport pathways into the Arctic and their connections to surface air temperatures". In: *Atmospheric Chemistry and Physics* 19, pp. 3927–3937. DOI: 10.5194/acp-19-3927-2019.

Mitchell, J. F. B., C. A. Senior, and W. J. Ingram (1989). "C02 and climate: a missing feedback?" In: *Nature* 341, pp. 132–134. DOI: 10.1038/341132a0.

Moss, R. et al. (2010). "The next generation of scenarios for climate change research and assessment". In: *Nature* 463. DOI: 10.1038/nature08823.

NASA (2024). *Climate Change*. URL: https://science.nasa.gov/climate-change/.

NASA Goddard Institute for Space Studies (2024). *GISS Surface Temperature Analysis (GISTEMP)*. URL: https://data.giss.nasa.gov/gistemp/.

Neale, R. et al. (2012). "Description of the NCAR Community Atmosphere Model (CAM5.0)". In: *NCAR Technical Note*. DOI: 10.5065/wgtk-4g06.

NOAA (2024). *National Snow and Ice Data Center*. URL: https://nsidc.org/home.

North, G. R., R. F. Cahalan, and C. J. A. (1981). "Energy balance climate models". In: *Reviews of Geophysics* 19.1. DOI: 10.1029/RG019i001p00091.

Notz, D. and J. Stroeve (2016). "Observed Arctic sea-ice loss directly follows anthropogenic CO2 emission". In: *American Association for the Advancement of Science*. DOI: 10.1126/science.aag2345.

Ono, J. et al. (2022). "Enhanced Arctic warming amplification revealed in a low-emission scenario". In: *Communications Earth & Environment* 3.1, p. 27. DOI: 10.1038/s43247-022-00354-4.

Parkinson, C. (2022). "Arctic sea ice coverage from 43 years of satellite passive-microwave observations". In: *Frontiers in Remote Sensing*. DOI: 10.3389/frsen.2022.1021781.

Payne, A. E., M. F. Jansen, and T. W. Cronin (2015). "Conceptual model analysis of the influence of temperature feedbacks on polar amplification". In: *Geophysical Research Letters* 42. DOI: 10.1002/2015GL065889.

Pendergrass, A. G., A. J. Conley, and F. M. Vitt (2017). "Surface and top-of-atmosphere radiative feedback kernels for CESM-CAM5". In: *Earth System Science Data* 9.1, pp. 517–524. DOI: 10.5194/essd-9-517-2017.

Pendergrass, A. G. (2017a). *CAM5 Radiative Kernels*. DOI: 10.5065/D6F47MT6. URL: https://doi.org/10.5065/D6F47MT6.

— (2017b). *CAM5 Radiative Kernels (GitHub repository)*. URL: https://github.com/apendergrass/cam5-kernels.

Perovich, D. et al. (2007). "Increasing solar heating of the Arctic Ocean and adjacent seas, 1979–2005: Attribution and role in the ice-albedo feedback". In: *Geophysical Research Letters* 34. DOI: 10.1029/2008GL034007.

Pharr, M. and G. Humphreys (2004). *Fundamentals of Rendering: Radiometry / Photometry*.

Pithan, F. and T. Mauritsen (2014). "Arctic amplification dominated by temperature feedbacks in contemporary climate models". In: *Nature Geoscience* 7, pp. 181–184. DOI: 10.1038/ngeo2071.

Polyakov, I. V. et al. (2017). "Greater role for Atlantic inflows on sea-ice loss in the Eurasian Basin of the Arctic Ocean". In: *Science* 356.6335. DOI: 10.1126/science.aai8204.

Previdi, M., K. Smith, and L. M. Lorenzo M Polvani (2021). "Arctic amplification of climate change: a review of underlying mechanisms". In: *Environmental Research Letters* 16. DOI: 10.1088/1748-9326/ac1c29.

Rantanen, M., A. Y. Karpechko, and A. Lipponen (2022). "The Arctic has warmed nearly four times faster than the globe since 1979". In: *Communications Earth & Environment* 3.1, p. 168. DOI: 10.1038/s43247-022-00498-3.

Ridley, J. K., M. A. Ringer, and R. M. Sheward (2016). "The transformation of Arctic clouds with warming". In: *Climatic Change* 139, pp. 325–337. DOI: 10.1007/s10584-016-1772-4.

Rose, B. E. J. et al. (2014). "The dependence of transient climate sensitivity and radiative feedbacks on the spatial pattern of ocean heat uptake". In: *Geophysical Research Letters* 41, pp. 1071–1078. DOI: 10.1002/2013GL058955.

Rousset, C. et al. (2015). "The Louvain-La-Neuve sea ice model LIM3.6: global and regional capabilities". In: *Geoscience Model Dev.* 8, pp. 2991–3005. DOI: 10.5194/gmd-8-2991-2015.

Schlichtholz, P., J. Marciniak, and W. Maslowski (2019). "Proxies for heat fluxes to the Arctic Ocean through Fram Strait". In: *Ocean modelling* 137, pp. 21–39. DOI: 10.1016/j.ocemod.2019.02.007.

Screen, A. J. and I. Simmonds (2010). "The central role of diminishing sea ice in recent Arctic temperature amplification". In: *Nature* 464, pp. 1334–1337. DOI: 10.1038/nature09051.

Screen, J. A., C. Deser, and I. Simmonds (2012). "Local and remote controls on observed Arctic warming". In: *Geophysical Research Letters* 39.10. DOI: 10.1029/2012GL051598.

Screen, J. et al. (2026). "Causes and consequences of Arctic amplification elucidated by coordinated multimodel experiments". In: *Communications Earth & Environment* 7, p. 23. DOI: 10.1038/s43247-025-03052-z.

Sellers, W. D. (1969). "A Global Climatic Model Based on the Energy Balance of the Earth-Atmosphere System". In: *Journal of Applied Meteorology and Climatology* 8.3. DOI: 10.1175/1520-0450(1969)008<0392:AGCMBO>2.0.CO;2.

Serreze, M. (2008). "Interactive comment on "The emergence of surface-based Arctic amplification". In: *The Cryosphere Discussions*.

Serreze, M. C. and R. G. Barry (2011). "Processes and impacts of Arctic amplification: A research synthesis". In: *Global and Planetary Change* 77, Iss. 1–2, pp. 85–96. DOI: 10.1016/j.gloplacha.2011.03.004.

Serreze, M. et al. (2026). "The Observed Evolution of Arctic Amplification over the Past 45 Years". In: *The Cryosphere* 20.1. DOI: 10.5194/tc-20-411-2026.

Shell, K. M. and C. A. Kiehl J.T.and Shields (2008). "Using the Radiative Kernel Technique to Calculate Climate Feedbacks in NCAR's Community Atmospheric Model". In: *Journal of Climate* 21, pp. 2269–2282. DOI: 10.1175/2007JCLI2044.1.

Sledd, A. et al. (2023). "Clouds Increasingly Influence Arctic Sea Surface Temperatures as CO2 Rises". In: *Geophysical Research Letters* 50.8. DOI: 10.1029/2023GL102850.

Smedsrud, L. H. et al. (2010). "Heat in the Barents Sea: transport, storage, and surface fluxes". In: *Ocean Science* 6, pp. 219–234. DOI: 10.5194/os-6-219-2010.

Smith, C. J. et al. (2020). "Effective radiative forcing and adjustments in CMIP6 models". In: *Atmospheric Chemistry and Physics* 20, pp. 9591–9618. DOI: 10.5194/acp-20-9591-2020.

Smith, D. et al. (2019). "The Polar Amplification Model Intercomparison Project (PAMIP) contribution to CMIP6: investigating the causes and consequences of polar amplification". In: *Geoscientific Model Development* 12.3, pp. 1139–1164. DOI: 10.5194/gmd-12-1139-2019.

Soden, B. J. and I. M. Held (2006). "An assessment of climate feedbacks in coupled ocean–atmosphere models". In: *Journal of Climate* 19.14, pp. 3354–3360. DOI: 10.1175/JCLI3799.1.

Soden, B. et al. (2008). "Quantifying Climate Feedbacks Using Radiative Kernels". In: *Journal of Climate* 21, pp. 3504–3520. DOI: 10.1175/2007JCLI2110.1.

Sperber, K. et al. (2013). "The Asian summer monsoon: an intercomparison of CMIP5 vs. CMIP3 simulations of the late 20th century". In: *Climate Dynamics* 41, pp. 2711–2744. DOI: 10.1007/s00382-012-1607-6.

Stock, C. A. et al. (2020). "Ocean biogeochemistry in GFDL's Earth System Model 4.1 and its response to increasing atmospheric CO2". In: *Journal of Advances in Modeling Earth Systems* 12. DOI: 10.1029/2019MS002043.

Stolla, M. K., H. Schmidt, and D. Notz (2023). "Understanding the Intermodel Spread of Simulated Arctic September Sea-Ice Sensitivity". In: *EGU General Assembly*. DOI: 10.5194/egusphere-egu23-8019.

Stommel, H. (1961). "Thermohaline Convection with Two Stable Regimes of Flow". In: *Tellus* 13.2. DOI: 10.1111/j.2153-3490.1961.tb00079.x.

Stroeve, J. C. et al. (2014). "Changes in Arctic melt season and implications for sea ice loss". In: *Geophysical Research Letters* 41.4, pp. 1216–1225. DOI: 10.1002/2013GL058951.

Subin, Z. M., W. J. Riley, and D. Mironov (2012). "Improved lake model for climate simulations". In: *Journal of Advances in Modeling Earth Systems* 4. DOI: 10.1029/2011MS000072.

Sweeney, A. J. et al. (2024). "Internal Variability Increased Arctic Amplification During 1980–2022". In: *Geophysical Research Letters*. DOI: 10.1029/2023GL106060.

Taylor, K. E. et al. (2007). "Estimating shortwave radiative forcing and response in climate models". In: *Journal of Climate* 20, pp. 2530–2543. DOI: 10.1175/JCLI4143.1.

Taylor, P. C. et al. (2013). "A Decomposition of Feedback Contributions to Polar Warming Amplification". In: *Journal of Climate* 26.18, pp. 7023–7043. DOI: 10.1175/JCLI-D-12-00696.1.

Taylor, P. C. et al. (2022). "Process Drivers, Inter-Model Spread, and the Path Forward: A Review of Amplified Arctic Warming". In: *Frontiers in Earth Science* 9, p. 758361. DOI: 10.3389/feart.2021.758361.

Tetzlaff, A. et al. (2013). "The impact of heterogeneous surface temperatures on the 2-m air temperature over the Arctic Ocean under clear skies in spring". In: *The Cryosphere* 7, pp. 153–166. DOI: 10.5194/tc-7-153-2013.

Timmermans, M. L. and J. Marshall (2020). "Understanding Arctic Ocean Circulation: A Review of Ocean Dynamics in a Changing Climate". In: *Advancing Earth and Space Sciences* 125.4. DOI: 10.1029/2018JC014378.

Vancoppenolle, M. et al. (2009). "Simulating the mass balance and salinity of Arctic and Antarctic sea ice. 1. Model description and validation". In: *Ocean Modellisation* 27, pp. 33–53. DOI: 10.1016/j.ocemod.2008.10.005.

Vavrus, S., M. M. Holland, and D. A. Bailey (2011). "Changes in Arctic clouds during intervals of rapid sea ice loss". In: *Climate Dynamics* 36, pp. 1475–1489. DOI: 10.1007/s00382-010-0816-0.

Vihma, T. (2014). "Effects of Arctic Sea Ice Decline on Weather and Climate: A Review". In: *Surveys in Geophysics* 35.5. DOI: 10.1007/s10712-014-9284-0.

Wagner, T. J. and I. Eisenman (2015). "How climate model complexity influences sea ice stability". In: *Journal of Climate* 28.10, pp. 3998–4014. DOI: 10.1175/JCLI-D-14-00654.1.

Wallace, J. M. and P. V. Hobbs (2006). *Atmospheric Science: An Introductory Survey*. 2nd ed. Amsterdam: Academic Press.

Weart, S. (2010). "The development of general circulation models of climate". In: *Studies in History and Philosophy of Modern Physics* 41, pp. 208–217. DOI: 10.1016/j.shpsb.2010.06.002.

Weber, S. L. (2010). "The utility of Earth system Models of Intermediate Complexity (EMICs)". In: *Climate Change* 1.2, pp. 243–252. DOI: 10.1002/wcc.24.

Wetherald, R. T. and S. Manabe (1988). "Cloud Feedback Processes in a General Circulation Model". In: *Journal of Atmospheric Sciences* 45.8. DOI: 10.1175/1520-0469(1988)045<1397:CFPIAG>2.0.CO;2.

Winton, M. (2006). "Amplified Arctic climate change: What does surface albedo feedback have to do with it?" In: *Geophysical Research Letters* 33.3. DOI: 10.1029/2005GL025244.

World Climate Research Programme (WCRP) (2026). *Coupled Model Intercomparison Project (CMIP)*. URL: https://wcrp-cmip.org/.

Xu, G. et al. (2024). "High-resolution modelling identifies the Bering Strait's role in amplified Arctic warming". In: *Nature Climate Change* 14, pp. 615–622. DOI: 10.1038/s41558-024-02008-z.

Ye, K. and G. Messori (2021). "Inter-model spread in the wintertime Arctic amplification in the CMIP6 models and the important role of internal climate variability". In: *Global and Planetary Change* 204. DOI: 10.1016/j.gloplacha.2021.103543.

Zelinka, M. D., S. A. Klein, and D. L. Hartmann (2012). "Computing and partitioning cloud feedbacks using cloud property histograms. Part II: attribution to changes in cloud amount, altitude, and optical depth". In: *Journal of Climate* 25, pp. 3736–3754. DOI: 10.1175/JCLI-D-11-00249.1.

Zhang, Y. et al. (2023). "Asymmetric Arctic and Antarctic Warming and Its Intermodel Spread in CMIP6". In: *Journal of Climate* 36.23. DOI: 10.1175/JCLI-D-23-0118.1.

Zhao, M. et al. (2018a). "The GFDL global atmosphere and land model AM4. 0/LM4.0: 1.Simulation characteristics with prescribed SSTs". In: *Journal of Advances in Modeling Earth Systems* 10, pp. 735–769. DOI: 10.1002/2017MS001208.

— (2018b). "The GFDL global atmosphere and land model AM4. 0/LM4.0: 2.Model description, sensitivity studies, and tuning strategies". In: *Journal of Advances in Modeling Earth Systems* 10, pp. 735–769. DOI: 10.1002/2017MS001209.